

Damage-based assessment of the risk of cut-out in trochanteric fractures for different PFNA blade positions

Francisco Maria Serra Rebelo de Andrade

Thesis to obtain the Master of Science Degree in

Mechanical Engineering

Supervisors: Prof. João Orlando Marques Gameiro Folgado
Prof. Carlos Miguel Fernandes Quental

Examination Committee

Chairperson: Prof. Paulo Rui Alves Fernandes
Supervisor: Prof. Carlos Miguel Fernandes Quental
Members of the Committee: Dr. Francisco Rosas Leitão Guerra Pinto
Prof. Rui Miguel Barreiros Ruben

November 2021

Acknowledgments

Em primeiro lugar, agradeço aos meus orientadores, Professor João Folgado e Professor Carlos Quental, pela oportunidade de desenvolver este tema e, principalmente, por todo o apoio incansável. A atenção e empenho com que acompanharam este trabalho e a disponibilidade total que mostraram para dar opiniões, esclarecer dúvidas e resolver problemas foram essenciais para a realização deste trabalho. Foi um privilégio poder trabalhar com os dois.

Agradeço ao Dr. Francisco Guerra Pinto por tudo o que me ensinou sobre anatomia e prática clínica e pela disponibilidade para responder às minhas dúvidas e receber-me no hospital, para me dar a conhecer o problema médico mais de perto.

Por último, agradeço à minha família e amigos por todo o apoio ao longo destes 5 anos de curso.

Resumo

O cut-out do parafuso de implantes da anca, definido como a perfuração da cabeça femoral devido ao colapso em varo do ângulo entre o pescoço e a diáfise, é a complicação mecânica mais comum no tratamento de fracturas trocantéricas. Um dos principais factores que influenciam o risco de cut-out é a posição do parafuso na cabeça femoral. Uma vez que a posição óptima do parafuso do PFNA nas direcções superior-inferior e medial-lateral não é conhecida, o objectivo deste trabalho foi investigar o impacto do posicionamento nestas direcções, usando modelos de elementos finitos de dois fémures com fracturas trocantéricas instáveis. Estes modelos foram combinados com um modelo de dano com adaptação de rigidez para avaliação do risco de cut-out. O parafuso foi colocado em cada modelo a quatro distâncias discretas da superfície da cabeça femoral – 5, 10, 15 e 20 mm – tanto em posições centrais como inferiores. A distribuição de dano no osso resultante do carregamento ao andar foi avaliada visual e quantitativamente, de modo a comparar o comportamento das oito posições e prever o risco relativo de cut-out para cada uma. Os resultados sugerem que quanto maior a profundidade de inserção do parafuso, menor o risco, ainda que não sejam recomendadas distâncias da ponta do parafuso à superfície da cabeça inferiores a 5 mm, e que a posição medial-lateral é mais relevante enquanto preditor do cut-out do que a posição superior-inferior. Foram também avaliados casos com carregamento excessivo, que mostraram grande impacto na propensão para o cut-out.

Palavras-chave: Cut-out, Dano, Fracturas trocantéricas, Método dos Elementos Finitos, PFNA

Abstract

Cut-out of the hip screw of fracture fixation implants, defined as the perforation of the femoral head by the screw due to the collapse of the neck-shaft angle into varus, is the most common mechanical complication in the treatment of trochanteric fractures. Among the factors that contribute to cut-out, the blade positioning in the femoral head is reported as one of the most relevant. Since the optimal blade position in the superior-inferior and medial-lateral directions is unknown, the goal of this work was to investigate the impact of blade positioning in these directions, using three-dimensional finite element models of two femora with unstable trochanteric fractures and eight different screw positions. These models were coupled with a stiffness-adaptive damage model for the evaluation of the risk of cut-out. The PFNA blade was placed in each model at four discrete distances from the femoral head surface – 5, 10, 15 and 20 mm – in both central and inferior positions. The damage distribution in bone resulting from a gait loading condition was visually and quantitatively assessed to compare the performance of the eight positions and predict the relative risk of cut-out for each. The results suggest that the deeper the blade, the lower the risk, although no tip-surface distances under 5 mm are recommended, and that the medial-lateral position is more relevant as a cut-out predictor than the superior-inferior position. Excessive loading conditions were also evaluated and were found to greatly impact the risk of cut-out.

Keywords: Cut-out, Damage, Finite Element Method, PFNA, Trochanteric fractures

Contents

Acknowledgments	i
Resumo	iii
Abstract	v
List of Tables	ix
List of Figures	xi
Nomenclature	xiii
Glossary	xv
1 Introduction	1
1.1 Motivation and goals	1
1.2 Thesis Outline	2
2 Background	5
2.1 Anatomical reference terminology	5
2.2 Hip joint anatomy	7
2.3 Proximal femoral fractures	9
2.3.1 Trochanteric fractures classification	11
2.3.2 Treatment	12
2.3.3 Main complications	15
2.4 Literature review	16
2.4.1 Cut-out	16
2.4.2 Bone damage models	19
2.5 Novel aspects of the work	20
3 Methods	23
3.1 Damage Model	23
3.2 Finite Element Model	24
3.3 Damage model and FEM integration	32
3.4 Analysis of results	34
3.4.1 Methods for damage model verification	34
3.4.2 Analysis of the risk of cut-out	35

4 Results	39
4.1 Damage model verification	39
4.2 Loading strategies evaluation	40
4.3 Assessment of the risk of cut-out	43
4.3.1 Damage distribution	43
4.3.2 Overload effect	43
5 Discussion	47
6 Conclusions and future work	51
References	53
A Minimum stiffness sensitivity analysis	63

List of Tables

2.1	Summary of the characteristics of some damage models present in the literature.	20
3.1	Damage model parameters.	24
3.2	Loads acting on the proximal femur.	31
4.1	DIVol evolution with iterations at full loading for the Minf5 and Finf10 models.	41

List of Figures

2.1	Anatomical positions and reference planes.	6
2.2	Illustrative schematic of varus and valgus conditions.	6
2.3	Hip joint anatomy.	7
2.4	Difference between cancellous and cortical bone on a proximal femur.	8
2.5	Anterior and posterior views of a right proximal femur.	8
2.6	Proximal femur muscle insertions.	9
2.7	Classification of proximal femoral fractures by location.	10
2.8	Boyd and Griffin classification system for extracapsular proximal femoral fractures.	11
2.9	Müller AO classification system for trochanteric proximal femoral fractures (31-A).	12
2.10	Evans-Jensen classification system for trochanteric proximal femoral fractures.	13
2.11	Dynamic Hip Screw implant.	14
2.12	Proximal Femoral Nail Antirotation implant.	14
2.13	X-ray of a hip screw cut-out on a proximal femoral fracture.	16
2.14	Technique for calculating TAD.	17
3.1	Three-dimensional geometric models of a male and a female right femora.	25
3.2	Geometric model of a female femur with a 31-A2.2 fracture.	26
3.3	Geometry of a real PFNA implant and 3D geometric model developed in Solidworks.	26
3.4	Representation of the eight configurations of the implant on the female bone.	27
3.5	Density distribution, in g cm^{-3} , on the osteoporotic female proximal femur model.	28
3.6	Shells simulating external cortical bone of the femur.	29
3.7	Attachment points for the application of loads in the female model.	30
3.8	Coordinate system used to describe the loading conditions.	31
3.9	Position of nodes and integration points in a C3D10 element.	31
3.10	Schematic of the algorithm implemented in MATLAB.	36
3.11	Schematic of the damage model algorithm implemented in MATLAB.	37
4.1	Comparison between the damage distribution on the Finf5 model, using minimum compressive principal strains higher than -0.84% as yielding criterion and the damage model implemented.	39
4.2	DIVol evolution on the Fcent20 model for different numbers of steps.	40

4.3	Comparison between the final damage distribution on the Finf20 model, for different numbers of load steps.	41
4.4	Damage distribution on the Finf10 and Minf5 models for both the full loading and the hybrid load application strategies.	41
4.5	Damage distribution on the Finf10 model for different load values.	42
4.6	DIVol evolution along the number of iterations in Finf10 using the full loading strategy. . .	42
4.7	Damage distribution on the female bone models.	43
4.8	Damage distribution on the male bone models.	44
4.9	DIVol for both the SP and IP of all geometries for the female and male models.	45
4.10	Comparison between the damage distribution on the Finf5 and Fcent20 model, using the normal loading scheme or a 100% overload.	46
5.1	Bone density, in g cm^{-3} , for male and female, central and inferior models.	48
A.1	Minimum stiffness sensitivity analysis.	63

Nomenclature

Greek symbols

α	Parameter for stiffness computation
ν	Poisson's ratio
ρ	Density
σ	Stress
σ_H	Hydrostatic stress
ε	Strain
ε_0	Yield strain
ε_f	Strain at fracture
ε_{eq}	Equivalent strain

Roman symbols

D	Damage variable
D_c	Critical damage
E	Young's Modulus
k	Maximum equivalent strain reached during loading history
n	Damage exponent
V	Volume

Subscripts

i	Computational index indicating integration point
i, j	Tensorial indexes

Superscripts

e	Computational index indicating element
-----	--

Glossary

3D	Three-dimensional
CaITAD	Calcar tip-apex distance
CDM	Continuum Damage Mechanics
CP	Convergence parameter
CT	Computed Tomography
DHS	Dynamic Hip Screw
FE	Finite Element
FEA	Finite Element Analysis
FEM	Finite Element Method
HU	Hounsfield Units
IP	Inferior part
NE	Number of elements
NIP	Number of integration points
ORIF	Open Reduction and Internal Fixation
PFNA	Proximal Femoral Nail Antirotation
SHS	Sliding Hip Screw
SP	Superior part
TAD	Tip-apex distance

Chapter 1

Introduction

This chapter presents a brief introduction to this work, presenting the motivation and goals. The outline of the document is also described.

1.1 Motivation and goals

Hip fractures are a common health problem among the elderly population all over the world, mainly due to the increasing aging of population and the prevalence of osteoporosis. These fractures present the highest rates of morbidity and mortality of all osteoporotic fractures. The main cause of hip fractures is low-impact trauma resulting from falls, representing 90-92% of fractures, and female patients are the most affected. It has been reported that approximately 20% of the patients die within 1 year of the fracture, and that only 40-79% regain their previous ambulatory function a year after the fracture, with less than half returning to their pre-fracture status of independence and daily activities [1–5].

Hip fractures occur on the proximal part of the femur, and may be divided into intracapsular or extracapsular, with the latter being subdivided into trochanteric and subtrochanteric fractures. They are influenced by hip anatomy, the hip joint forces and bone mechanical properties. The treatment of hip fractures is mainly surgical, representing a large part of the orthopedic surgery activity, and have associated high clinical and social cost implications. For most cases, fractures are stabilized using either intra- or extramedullary fixation devices, generally composed of a rod placed along the femoral shaft and a screw or a blade crossing the femoral head; the most common are, respectively, the Proximal Femoral Nail Antirotation (PFNA) and the Dynamic Hip Screw (DHS). Although allowing a stable fixation in the majority of cases, there is still a significant number of post-operative complications reported, compromising the success of the procedure. The hip screw cut-out, defined as the collapse of the neck-shaft angle into varus leading to extrusion of the screw from the femoral head, is the most common mechanical complication, accounting for 85% of fixation failures. This phenomenon occurs in between 1.1% to 6.3% of all patients with trochanteric fractures. Other common complications have to do with mal-union or non-union of the fracture fragments, femoral shaft fracture or implant failure. Several factors may affect the risk of cut-out, including the patient's age and sex, bone quality, fracture pattern and stability, quality

of reduction, the neck-shaft angle of the fixation device and its design, and the screw positioning in the femoral head [1, 6–9].

The screw position has been frequently discussed in the literature, with several authors focusing on its biomechanical effect in both clinical and computational studies; however, there has been no clear consensus about the optimal position to reduce the risk of cut-out [9]. Many clinical studies evaluated the position of the screw immediately after the surgery and after a follow-up period, performing statistical studies to find relations between the post-surgical position and the risk of cut-out [10–14]. On the other hand, computational studies have been using finite element models for different screw positions, evaluating mainly the stress and strain distribution to conclude about the position that leads into less bone damage [8, 15–19]. While it is consensual that the central position in the anterior-posterior direction is the less prone to cut-out, findings about the position in the other directions are contradictory. In the superior-inferior direction, literature conclusions are divided between central and inferior positions. For the medial-lateral directions, while there are few studies that focus on the position in this direction, surgical technical guides suggest a 10 mm direction between the tip of the screw and the femoral head surface, measured in a straight line along the axis of the screw [20]. Baumgaertner et al. [21] have proposed a measure, the tip-apex distance (TAD) – the distance from the tip of the screw and a point in the femoral head surface, measured in both anteroposterior and lateral views – to evaluate the risk of cut-out, arguing that a lower TAD led to a lower risk. However, while some authors supported this finding, others have shown opposition to it.

The goal of this work is to contribute to the investigation on the optimal position for the PFNA blade in the superior-inferior and medial-lateral directions, using three-dimensional finite element models of two femora with unstable trochanteric fractures and eight different screw positions, varying both the superior-inferior position and the depth of insertion of the screw. These models were coupled with a damage model for the evaluation of the risk of cut-out. Another goal is to study the influence of the loading intensity on the risk of cut-out.

1.2 Thesis Outline

This work is divided into six chapters. This first chapter is an introduction, where the motivation, purpose of this work and outline of this document are described.

Chapter 2 provides an overview of the anatomy concepts necessary to understand this work. It also introduces technical and clinical information on proximal femoral fractures classification and treatment, including the recommended surgical procedure and the main complications. Finally, literature reviews on cut-out and damage models are presented.

In Chapter 3, the methodology used in this work is described, namely the damage model used to evaluate bone damage and update the stiffness accordingly, the finite element models developed and the way these models are coupled and implemented. The quantitative parameters used to evaluate the risk of cut-out for the different bone configurations are described. Afterwards, the simulations performed are described.

Chapter 4 starts with a verification of the damage model behaviour, followed by the results used to choose the load application strategy to be used for the other simulations. Finally, the results obtained in the analyses are presented, being discussed and compared to the literature in Chapter 5.

Finally, Chapter 6 includes the conclusions of this study, also presenting some suggestions for future work that could advance this study.

Chapter 2

Background

This chapter starts by introducing anatomical concepts of the human body and, in particular, about the hip joint and the proximal femur. A theoretical overview about proximal femoral fractures and their classification and treatment is presented, along with an overview of the main complications that results from these injuries. Literature reviews on the screw cut-out complication and damage models are provided. Finally, the novel aspects of the present work and its contribution to the state of the art are described.

2.1 Anatomical reference terminology

To study the anatomy of the human body, reference terminology is used to define body positions and directions. The anatomical reference position is the position in which the body is standing upright with feet together, hands by the side and face looking forward. The palms of the hands are facing forward with the fingers straight and together, and the pad of the thumb is turned 90° with the pads of the fingers. The toes must be pointing forward. With the body in this position, three major planes are defined: the coronal or frontal plane is oriented vertically and divides the body into anterior and posterior parts; the sagittal plane is also oriented vertically but is at right angles with the coronal plane, dividing the body into right and left parts; and the transverse, horizontal or axial plane, that is at right angles with the two previous ones and divides the body into superior and inferior parts [22]. All these planes bisect the mass of the body, and intersect on the body's center of mass. The anatomical reference position and planes are illustrated in Figure 2.1.

To describe location on the human body, four major dichotomies are used: anterior and posterior describe positions relative to the front and back of the body, respectively, being associated with coronal planes; medial and lateral describe the position of a structure closer and farther to the sagittal plane, respectively; superior refers to a position towards the head, while inferior means the opposite; and proximal and distal are used with reference to being, respectively, closer or farther from the trunk, not being directly related to any of the anatomical reference planes [22, 23]. These anatomical directions are also represented in Figure 2.1.

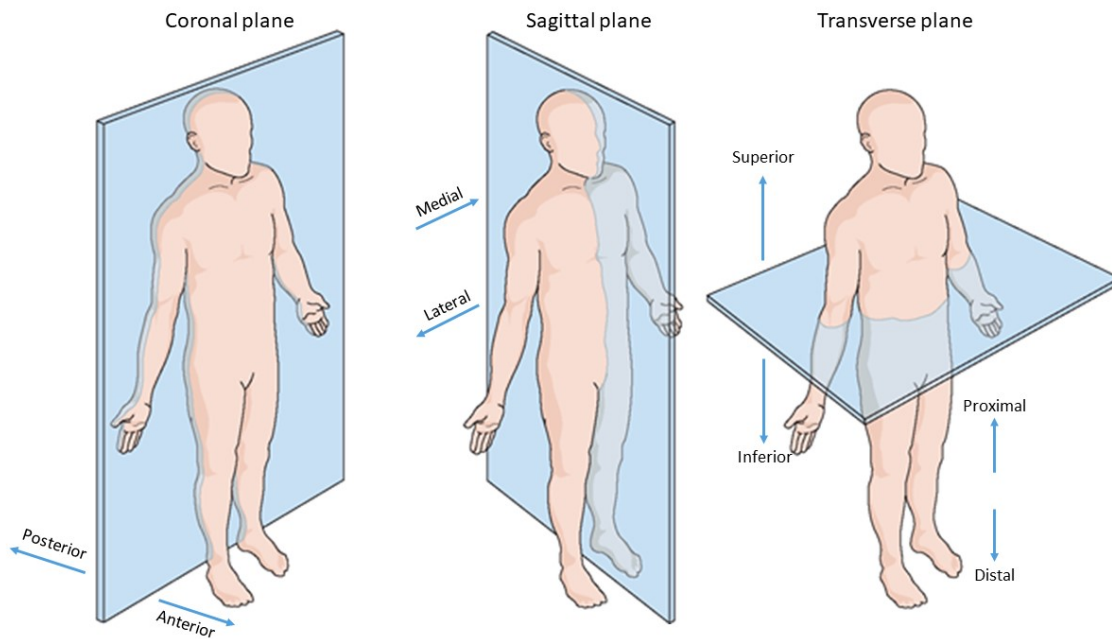


Figure 2.1: Anatomical positions and reference planes. Adapted from [24].

Another important pair of concepts in anatomy are varus and valgus conditions, which indicate, respectively, inward and outward lateral deviation of a body segment, with the distal part being more medial or lateral than in the normal configuration, leading to angulation [23]. As an example, Figure 2.2 illustrates the concepts on a femur and tibia.

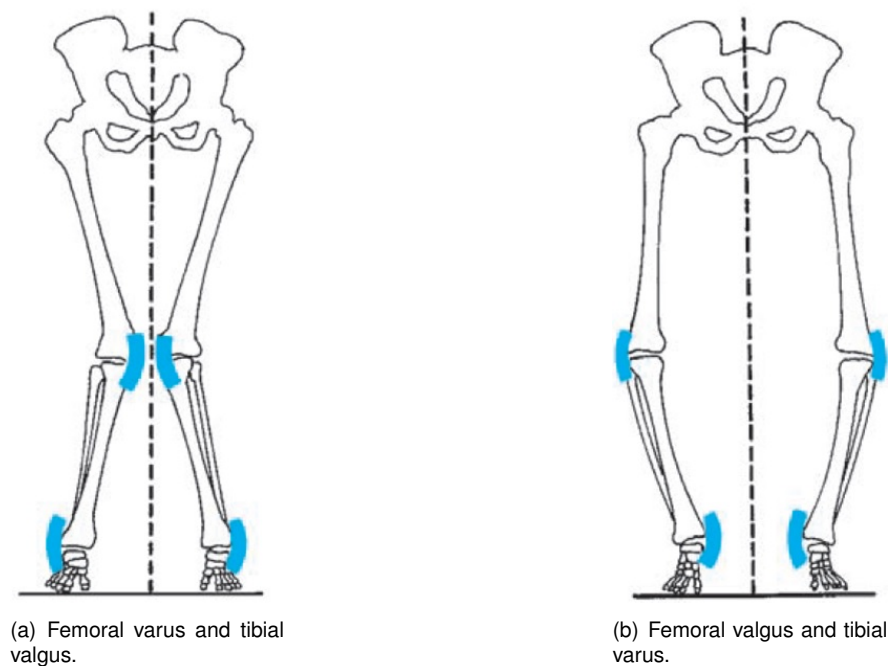


Figure 2.2: Illustrative schematic of varus and valgus conditions.

2.2 Hip joint anatomy

The hip joint, pictured in Figure 2.3, is a ball and socket joint that articulates the head of the femur with the acetabulum of the pelvis. The acetabulum is a cup-like depression on the pelvic bone, where the head of the femur fits completely [25]. The hip joint's primary function is to provide dynamic support to the body while facilitating load transmission from the skeleton to the lower extremities, allowing mobility. The joint is covered by articular cartilage, a connective tissue with the function of providing a smooth, lubricated surface for articulation and to facilitate the transmission of loads with a low frictional coefficient [26].

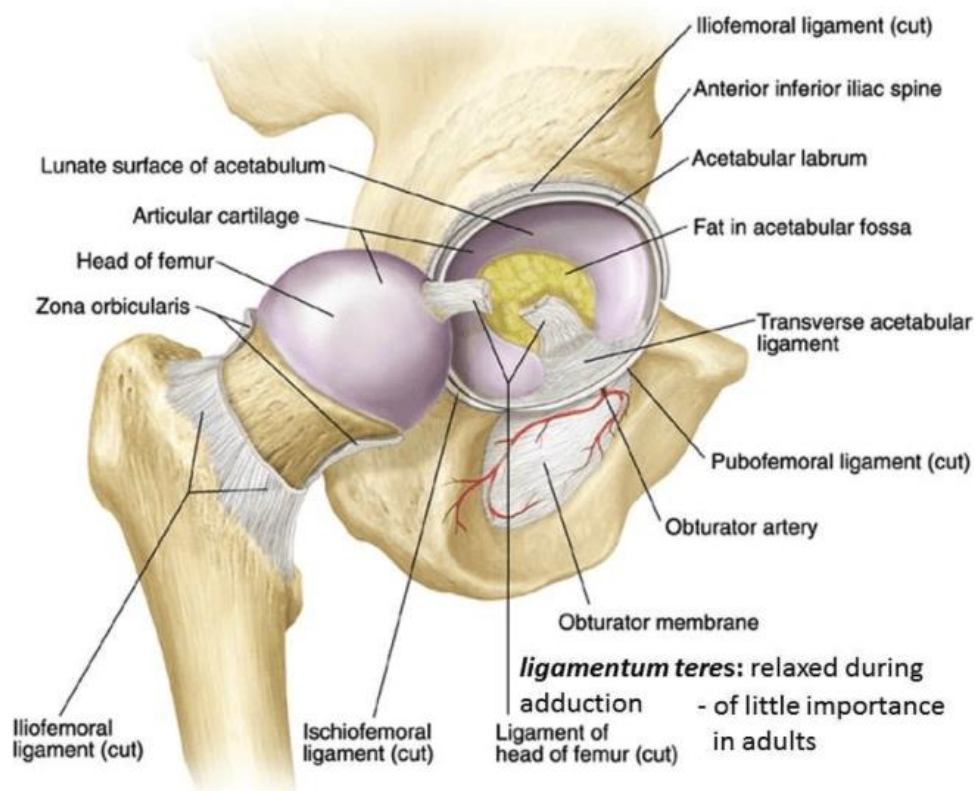


Figure 2.3: Hip joint anatomy [27].

Bone tissues, like the femur and pelvis, have particular structural properties: compression strength and stiffness are provided by inorganic components, while organic components provide tensile strength and stiffness. Also, bone tissue is a non-homogeneous, porous and anisotropic material. It can be distinguished between two types: trabecular or cancellous bone, formed by several trabeculae around 50-300 μm thick that assemble to form foam-like structures with 70-95% porosity; and cortical bone, which constitutes compact shells with thicknesses from tenths of the millimeter to a few millimetres and a low porosity of 4-17%. Within the trabecular bone, a semi-solid tissue named bone marrow is stored. The difference between these two types of bone is illustrated in Figure 2.4. Another characteristic of bone tissue is its capability to adapt to loading and self-repair when damaged. This process is called bone remodelling and has been modelled by many authors [28, 29].

The femur, located in the thigh, is the longest bone in the human body. Its head is spherical and has

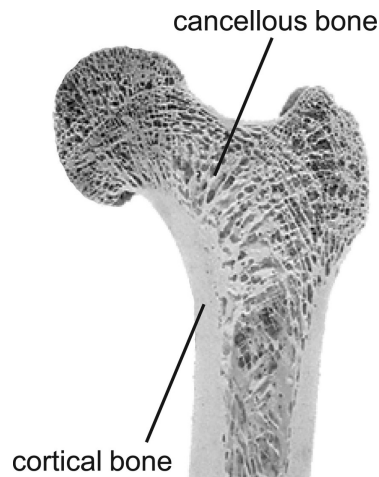


Figure 2.4: Difference between cancellous and cortical bone on a proximal femur [30].

a nonarticular pit (fovea) on its medial surface for the attachment of the ligament of the joint. The neck of the femur is a cylindrical structure that connects the head to the shaft, forming an angle of approximately 125° , which increases the possible range of movement of the hip joint. Figure 2.5 illustrates the anatomy of the proximal femur.

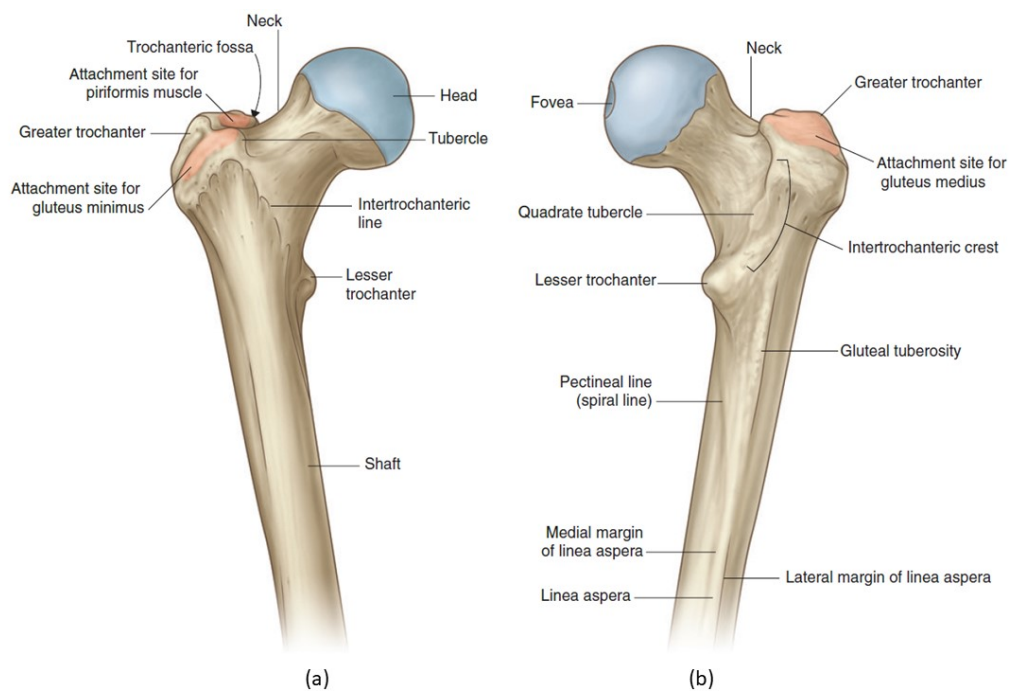


Figure 2.5: Anterior (a) and posterior (b) views of a right proximal femur. Adapted from [22].

The proximal femur has 2 projections, the greater and lesser trochanters, which are attachment sites for muscles. The greater trochanter extends superiorly from the shaft, lateral to the region where the shaft and neck join. The projection continues in the posterior direction to the trochanteric fossa. It also has two ridges on its anterolateral and lateral surfaces, for attachment of muscles. The lesser trochanter projects posteromedially from the shaft just inferior to the junction with the neck. The intertrochanteric

line and crest extend between the two trochanters. The shaft descends from medial to lateral along the coronal plane, describing a 7° angle with the vertical axis. The shaft is hollow inside, with a cavity called the medullary cavity, where bone marrow is stored [22].

Forces on the femur are exerted by muscles and the contact at the hip joint. Figure 2.6 illustrates the muscle attachments on the proximal femur. These muscles are divided into three groups: (i) the hip flexor muscles (pectineus, iliopsoas, psoas minor, iliacus, sartorius, and quadriceps), which arise from the acetabulum, spine and proximal femur; (ii) the medial or adductor muscles (adductor magnus, adductor longus, adductor brevis, gracilis, and obturator externus), which connect to the anteroinferior external surface of the pelvis; and (iii) the hip extensor muscles (semitendinosus, semimembranosus, and biceps femoris), which are attached to the medial tibia and lateral fibula [31]. The most relevant muscles for walking are the gluteus minimus, medius and maximus, the tensor fasciae latae and the vastus lateralis [32].

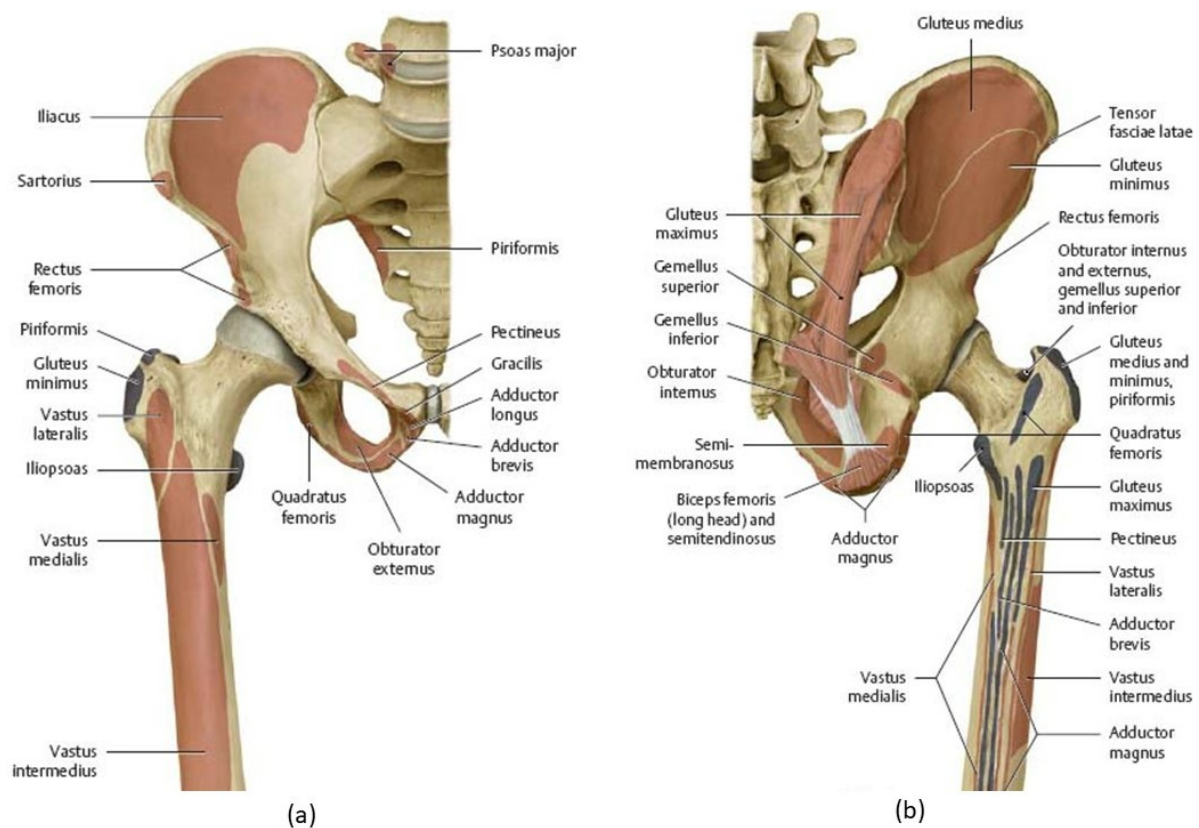


Figure 2.6: Proximal femur muscle insertions [33]. (a) Anterior view; (b) Posterior view.

2.3 Proximal femoral fractures

Hip fractures represent around 25% of the geriatric fractures requiring hospital admission. They occur most frequently on patients older than 65 years old suffering from other medical comorbidities. Its morbidity and mortality, in spite of the enhancements in medical services over the last years, remain elevated [6].

Proximal femoral fractures are the most common type of hip fractures, and occur anywhere between the edge of the femoral head and 5 cm below the lesser trochanter. These fractures may be divided into two groups according to their location: intracapsular or extracapsular, with the latter being further subdivided into trochanteric (or intertrochanteric) and subtrochanteric [34, 35]. Figure 2.7 illustrates the classification of proximal femoral fractures based on their location. In this work, only extracapsular fractures will be addressed.

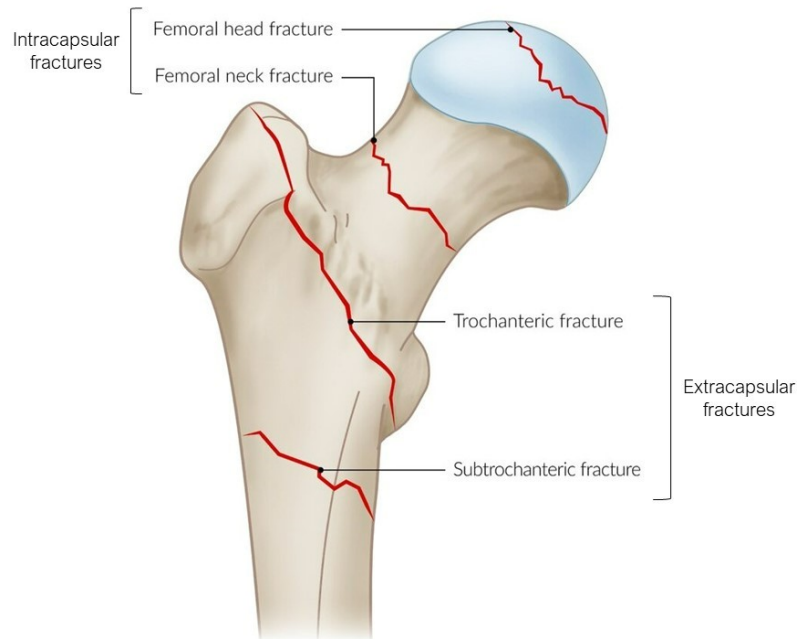


Figure 2.7: Classification of proximal femoral fractures by location. Adapted from [36].

Subtrochanteric fractures constitute 10-30% of all proximal femoral fractures and occur below the lesser trochanter [34]. The treatment of these fractures has been proven difficult, due to several factors: a high biomechanical stress concentration in this region during normal weight bearing; competing forces exerted by muscular attachments, causing misalignment of the fractures fragments; and a predominance of cortical bone in this zone, implying a weaker vascularization, thus slowing down the consolidation of the fracture. Subtrochanteric fractures tend to happen more frequently in three different population groups: patients under 50 years old with high-energy trauma; elderly patients with osteoporotic bones with low-energy trauma; and patients under long duration pharmacologic treatment, resulting in impaired bone remodeling [37–39].

Trochanteric or intertrochanteric fractures occur in the area between the greater and lesser trochanter, which may also be involved. When the fracture involves both trochanters, with one or both being fractured, it is called a pertrochanteric fracture. This is the most common type of hip fracture, accounting for 45% of the cases, and are most commonly seen in the elderly, mainly on women older than 60 years old. These fractures usually occur following a lateral fall with impact on the greater trochanter. Osteoporosis plays a major role on both the fracture risk and severity, as does the direction of the impact. Due to the region where they happen, being composed of weight bearing trabeculae and having good vascularity, the risks of necrosis and non- or mal-union are minimal [34, 37]. Henceforth, the present study will focus

on this type of fractures.

2.3.1 Trochanteric fractures classification

The classification of extracapsular fractures has been evolving since Boyd and Griffin [40] in 1949. They classified these fractures into four types, which are depicted in Figure 2.8. Type I fractures present a regular fracture along the intertrochanteric line, and reduction – setting the bone fragments back to their correct position – is simple. Type II fractures are comminuted and present multiple breaks in the cortex, despite the main line still being along the intertrochanteric line; reduction is more difficult. Type III designates subtrochanteric fractures with at least one fracture line passing across the upper end of the shaft or around the lesser trochanter, being much more difficult to reduce. Type IV fractures are comminuted fractures involving both intertrochanteric and subtrochanteric regions, with fractures lines in at least two planes [40, 41].

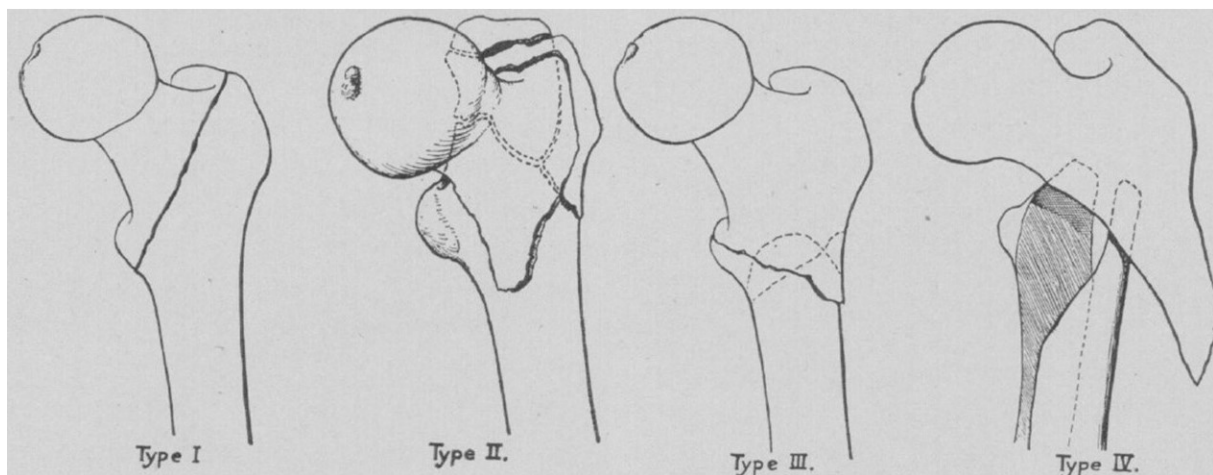


Figure 2.8: Boyd and Griffin classification system for extracapsular proximal femoral fractures. Adapted from [40].

Several authors have later developed classification systems for this type of fractures. The most used is the AO classification system, published by Müller et al. [42] in 1990, which is a fracture classification system for long bones fractures. The first digit of the classification refers to the bone, 3 being the femur, and the second digit indicates the segment as proximal (1), diaphyseal (2) or distal (3). The letter A, B or C provides information on the type of fracture, which in the proximal femur case may be an extraarticular fracture on the trochanteric area, an extraarticular fracture on the femoral neck or an articular fracture on the femoral head, respectively. Finally, for trochanteric fractures (31-A), 9 configurations are possible, defined by two digits. The first one defines the group of fractures, between simple pertrochanteric two-part fractures (1), multifragmentary pertrochanteric fractures (2) and intertrochanteric fractures of different morphologies, including reverse oblique and transverse patterns (3). The second digit describes the subgroup, as shown in Figure 2.9.

Evans [43] developed another widely used classification system that divides fractures into two types: type 1, in which the fracture line runs upwards and outwards from the region of the lesser trochanters;

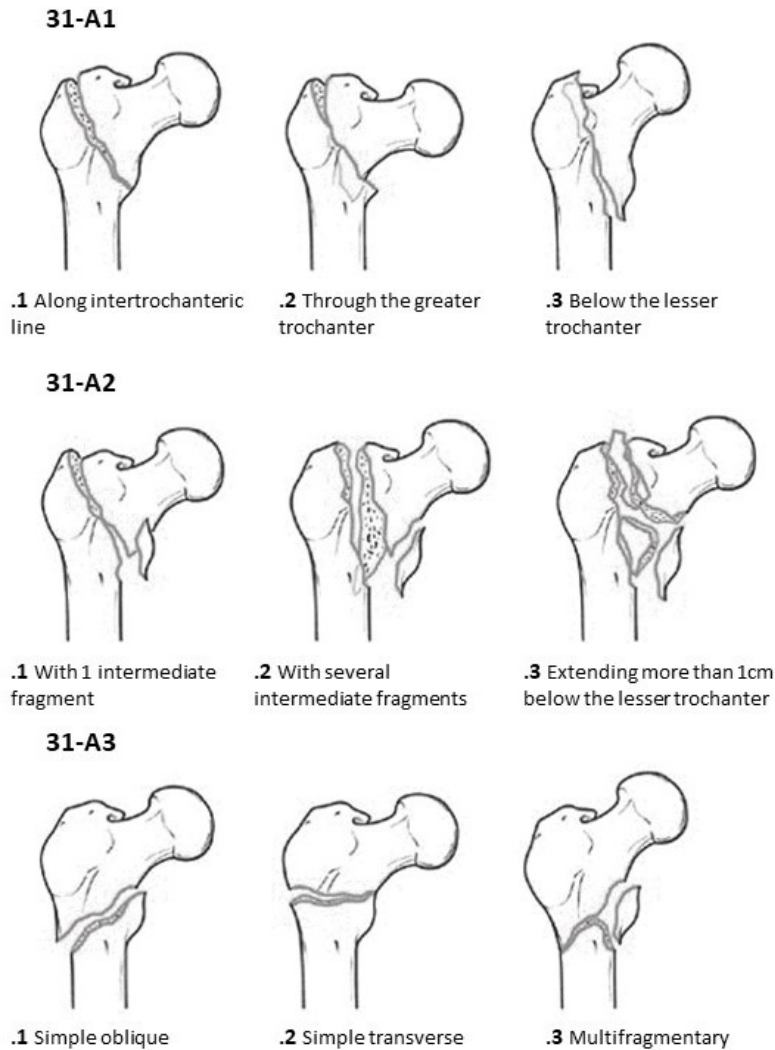


Figure 2.9: Müller AO classification system for trochanteric proximal femoral fractures (31-A). Adapted from [42].

and type 2, with an 8% incidence, in which the line is the reverse of that usually found. This system was later modified by Jensen and Michaelsen [44], originating the Evans-Jensen system. It divides the fractures into 5 types, illustrated in Figure 2.10. The main purpose of this system is to predict whether the fracture will be stable after reduction or will be unstable, displacing after the procedure.

2.3.2 Treatment

Trochanteric fractures present a risk of complications and loss of independence and walking capability in the elderly. To reduce these risks, health professionals must choose a treatment allowing verticalization and early sitting, involving as little shock, surgery time and blood loss as possible, in order not to impact recovery [45]. The treatment must provide a stable fixation to allow immediate weight bearing, while minimizing potential for implant failure and maximizing potential for recovering the patients' pre-fracture mobility [46].

Treatment for trochanteric hip fractures can be of three types: functional treatment, conservative

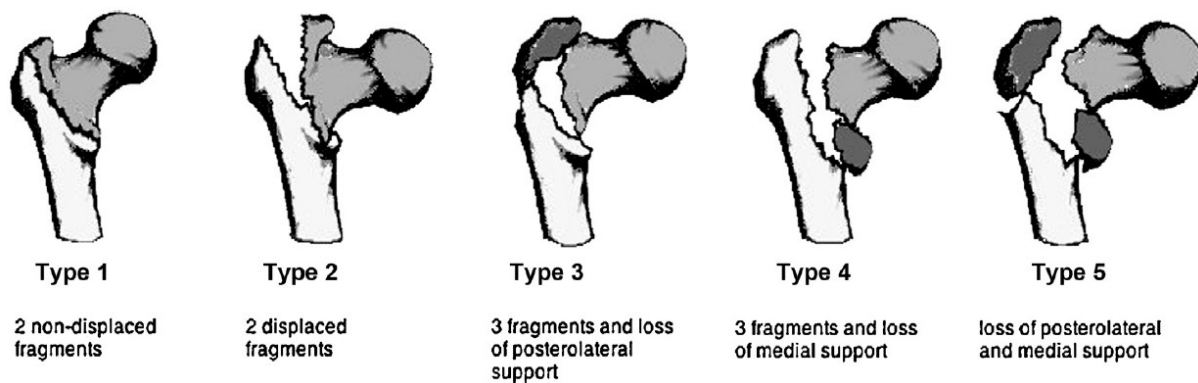


Figure 2.10: Evans-Jensen classification system for trochanteric proximal femoral fractures [45].

treatment or surgical treatment. The first two types of treatment are mainly for patients with absolute anesthesiological or surgical contra-indication, and present high risks of secondary displacement and loss of independence in the elderly. Surgical treatment is, by far, the most common type of treatment, and is performed as quickly as possible after stabilization of vital functions [45].

The surgical procedure comprises two phases: reduction and fixation. Open reduction and internal fixation (ORIF) is the most frequent attitude in these fractures, using intra- or extramedullary implants. Trochanteric fractures surgeries are frequent and considered to be simple, often being performed by less experienced surgeons [45].

The most used implant with extramedullary fixation is the Dynamic Hip Screw (DHS), pictured in Figure 2.11. The DHS consists of a lag screw and a plate with a barrell in which the lag screw can glide. The plate is fixed in the external surface of the bone, using 4.5 mm screws. It is designed to provide strong and stable internal fixation of a variety of fractures. This implant offers good results for stable fractures with little displacement; however, for unstable fractures, a higher incidence of failure when compared to intramedullary implants has been reported, particularly in cases with no posteromedial support [10, 47].

To overcome some surgical complications found within the treatment with the DHS, intramedullary implants were developed. The most used intramedullary implant is the Proximal Femoral Nail Antirotation (PFNA). The PFNA implant consists of three parts: the intramedullary nail; the helical blade (substituting DHS' lag screw), which increases the contact area between bone and implant, improving attachment; and the distal locking screw. Nail-blade angle is variable and must be chosen according to the fracture geometry. Several authors have reported better results for this implant than the DHS, especially in unstable fractures [47, 49–51]. There are some implants similar to the PFNA, e.g. Stryker's Gamma nail, the Targon PF, among others.

The surgical procedure for insertion of the PFNA is detailed on the surgical technique guide developed by the manufacturer DePuy Synthes [20]. The first step is to reduce the fracture. A closed reduction using the traction table is initially attempted. If the initial result is not satisfactory, an open reduction is necessary. After confirming the quality of the reduction by medical imaging, an incision 5 cm proximal from the tip of the greater trochanter, found by palpation, is made. The entry point for the

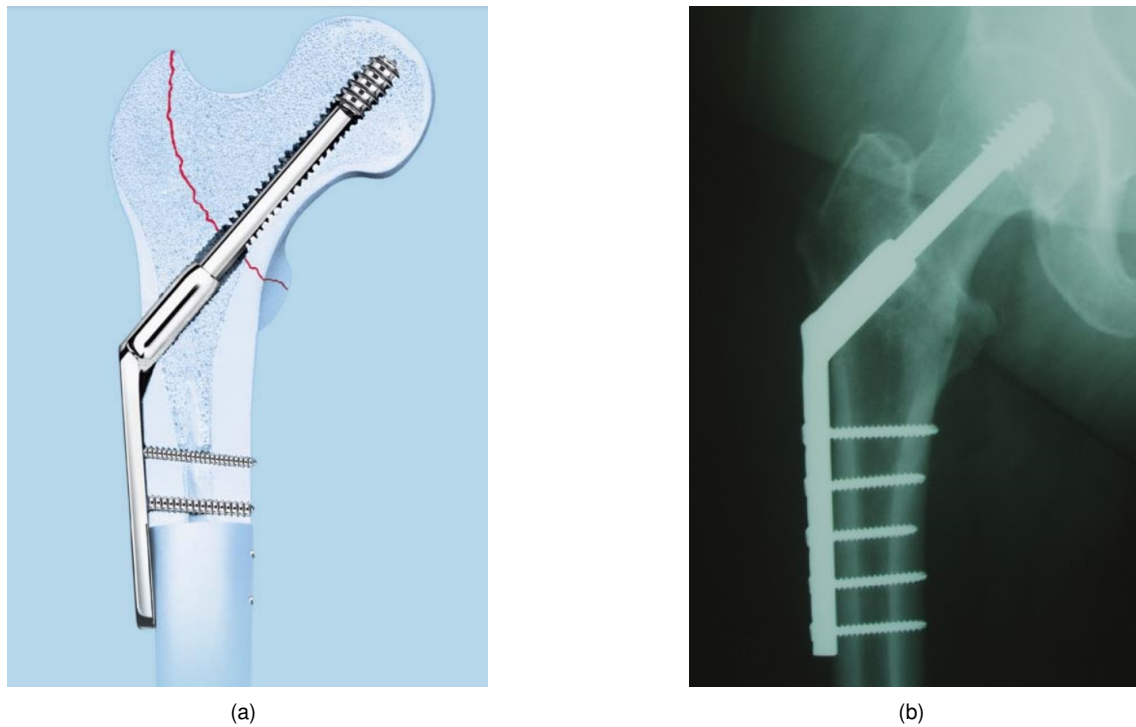


Figure 2.11: Dynamic Hip Screw implant [48]. (a) Illustrative image; (b) X-ray image.

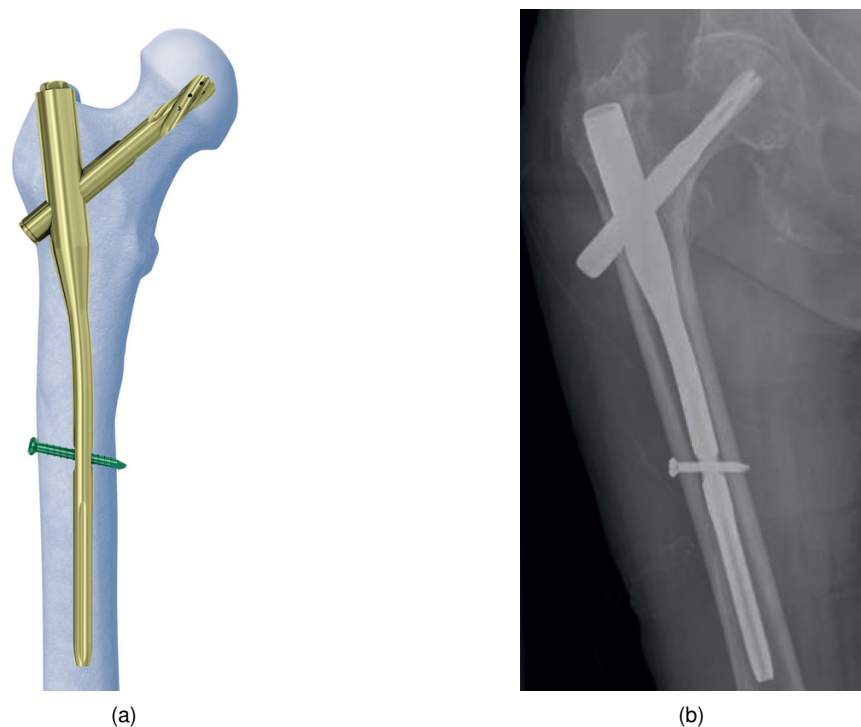


Figure 2.12: Proximal Femoral Nail Antirotation implant [20]. (a) Illustrative image; (b) X-ray image.

PFNA is the tip of the greater trochanter, in line with the axis of the medullary cavity in the lateral view, and the entry orientation is chosen to create an angle of 6° with the femoral shaft in the anteroposterior view. Found the entry point, the guide wire is inserted laterally and the femur is opened using a drill. The nail is inserted, its position being controlled by x-ray images. Afterwards, using an aiming arm, a

new guide wire is inserted, a hole is drilled from the lateral cortex, and the blade is inserted. While being inserted, the blade works as a drill; when the desired position is obtained, the blade is locked to activate its antirotation feature. Finally, a similar procedure is followed for the insertion of the locking screw. Two distal locking strategies are available: dynamic locking (allowing for small movements of the nail) or static locking. After the distal screw insertion, surgery is complete.

Shortly after the surgery, some degree of weight bearing is essential to activate biological mechanisms for bone healing. Also, biomechanically, the absence of weight bearing causes the effective center of gravity of the patient to move distally and away from the injured leg, increasing abductor muscle forces, which results in severe joint compression forces [52].

2.3.3 Main complications

Medical complications affect around 20% of patients with hip fractures, with a wide range going from cognitive and neurological alterations to electrolytic and metabolic disorders. Surgical complications after hip fractures are fairly common, and vary depending on the location of the fracture. Intracapsular fractures tend to have mostly biological problems, related to poor vascularization in the femoral head. On the other hand, in extracapsular fractures, most problems are mechanical, related to load-bearing. The most common mechanical complications in this type of fractures are screw cut-out, femoral shaft fracture and implant failure [6].

Cut-out is defined as the collapse of the neck-shaft angle into varus, giving rise to an oblique displacement and/or rotation of the femoral head, thus causing damage to the trabecular bone, and facilitating the displacement of the cephalic screw and its extrusion from the femoral head [8, 9]. It is the main mechanical surgical complication in hip fractures, with an incidence as high as 8% for all fractures treated with hip screws [53].

Femoral shaft fractures occur mainly in patients with first-generation intramedullary nails, which have a larger distal diameter - patients with these nails present a 5.3% shaft fracture rate [6]. Second-generation intramedullary nails, with smaller distal diameters and reduced valgus offset, caused a substantial reduction of the incidence of this type of complication.

Implant failure usually derives from poor fracture reduction, high mechanical stresses or fracture instability, but may also be caused by technical errors during the surgical procedure. It has been reported that the greater the rigidity of the fracture fixation device, the higher the incidence of implant failure [6].

Other surgical complications have also been reported by several authors (e.g. Eberle et al. [7], Guerra Pinto et al. [54], Unger et al. [55], Papasimos et al. [56]). These less frequent complications include loss of reduction, cephalic penetration, mal-union or non-union of the bone and fracture of the greater trochanter.

2.4 Literature review

In this section, the state of the art on the assessment of the risk of cut-out of the hip screw complication and literature review on bone damage models are presented.

2.4.1 Cut-out

This work focuses on the cut-out of the hip screw, which is the most frequent complication in the treatment of proximal femoral fractures. It is estimated to occur in 1.1% to 6.3% of patients with extra-capsular fractures, and represents 85% of fixation failures [6]. This phenomenon leads to a reduction of the neck-shaft angle, leading for the tip of the lag screw perforating the femoral head. Figure 2.13 shows an x-ray image of a proximal femur presenting cut-out. The white arrow points to the initial position of the screw.



Figure 2.13: X-ray of a hip screw cut-out on a proximal femoral fracture [57]. The white arrows indicates the screw position after the surgery.

Cut-out risk is influenced by patient's age, bone quality, fracture pattern and stability, quality of reduction, the neck-shaft angle of the fixation device and its design, and the screw/blade positioning in the femoral head. There is a high incidence of osteoporosis in the patients where this complication arises. Type 31-A2 fractures are the most common, with Caruso et al. [58] reporting this type of fractures to account for 57% of all fractures in patients with cut-out. Valgus reductions were reported to lead to a

lower risk of cut-out [59]. Frequent discussion exists in the literature about the interrelationships and relative importance of each of these factors and, although there is no clear consensus yet, most authors have recognized the importance of accurate placement of the screw [9, 21].

In 1995, Baumgaertner et al. [21] proposed using the distance between the screw tip and the apex of the femoral head (the point of intersection between the subchondral bone and a line representing the axis of the femoral neck), named tip-apex distance (TAD), as a predictor of the risk of cut-out. This measure provides a single number that summarizes the position and depth of the lag screw on both anteroposterior and lateral views, and is defined as the sum of that distance in both views. Figure 2.14 illustrates the definition of TAD.

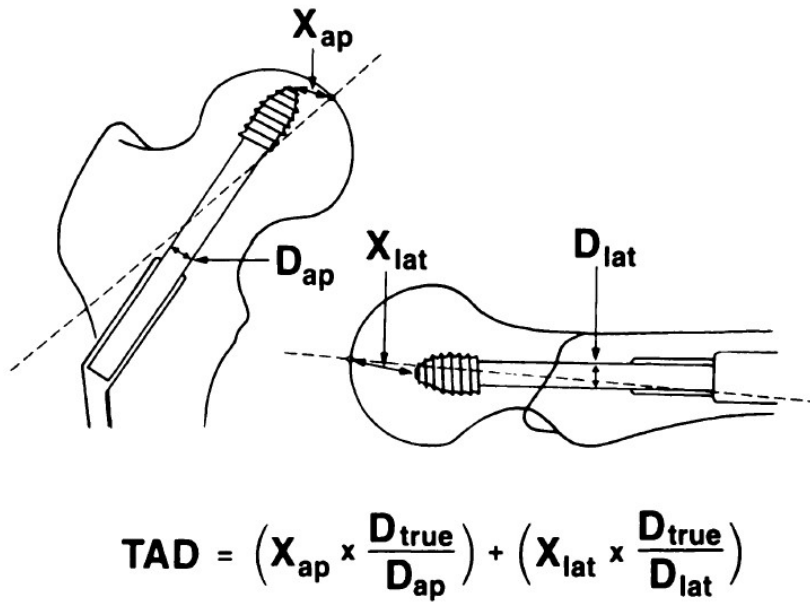


Figure 2.14: Technique for calculating TAD [21]. D_{true} is the true diameter of the hip screw, and D_{ap} and D_{lat} are the diameter values directly measured on the radiography. The diameter fractions are multiplied for each distance to achieve the real value from the magnified one obtained from the images.

Baumgaertner et al. concluded in their study that the increasing TAD was highly correlated with an increasing rate of cut-out, regardless of any other variables that may be involved on the fracture [21]. Later, many other studies have reached controversial results: some works indicated the same positive correlation between TAD and cut-out [10], while others found no direct relationship [60].

In 2012, Zuzyk et al. [61] developed a new measure, called calcar-TAD (CalTAD), using as reference a point in line with the femoral calcar, a plate of dense trabecular bone placed in the posterior femoral neck, instead of the neck axis. The distance on the lateral view remains unchanged, but the distance on the antero-posterior view is measured from the tip of the screw to the new point. There is no consensus on whether the CalTAD is a better or worst predictor of cut-out than the TAD.

Regarding the screw position, the screw tip must be placed centrally in the anterior-posterior direction and centrally or inferiorly in the superior-inferior direction, since clinical studies showed that other positions lead to much higher cut-out rates [10–14].

Recently, several authors have tried to evaluate the risk of cut-out using computational finite element

analyses. In order to evaluate the influence of the screw position on the femoral head, Arias-Blanco et al. [8] developed a finite element model of a femur with a stable 31-A1 fracture and a PFNA implant, with only one force applied on the femoral head. They evaluated the von Mises stress in the fixation device, the minimum principal stress of the trabecular bone, the global stiffness of the bone-implant system and the torsional moment experienced by the hip screw. This study concluded that the screw should be positioned in a central-central position, by arguing that, although the inferior position was slightly less prone to cut-out, it increased the load on the implant and the torque on the screw. Lee et al. [15] performed a similar analysis for 5 different blade positions, using a more realistic loading model, and also evaluated the normal strains in the fracture surface, since normal compressive strain is usually beneficial for bone healing. This work concluded that the inferior position is preferred, although a posterior-central position for the blade is also acceptable. Also, Lee et al. argued that TAD is not a good predictor for cut-out. Celik et al. [16] studied a DHS implant instead of a PFNA, taking similar conclusions. Liang et al. [17] analysed a PFNA implant, concluding once again that the screw must be placed as deep as possible, corroborating the TAD theory. They also defended that the lag screw must be placed in the inferior region, allowing it to sustain greater stresses. Goffin et al. [18] evaluated nine different configurations for bones treated with a sliding hip screw (SHS), placing the hip screw from anterior to posterior and from inferior to superior. Assessing the minimum principal strains, and relating the volume of elements with compressive strains over the yield strain with the risk of cut-out, they concluded that the safest positions are central-inferior and posterior-inferior. This work also suggested that TAD is not an accurate predictor of cut-out. Finally, Quental et al. [19] evaluated the risk of cut-out in central-central and central-inferior positions. They also tested several depths of the blade - for both cases, distances of 5, 10, 15 and 20 mm from the tip of the blade to the external surface of the femoral head were evaluated. Quental et al. resorted to minimum principal strains to assess the risk of cut-out, concluding that central-inferior positions were safer, and the optimal distance was of 10 mm.

Another factor that may influence the risk of cut-out is the type of implant used for surgical fixation. Several clinical studies have focused on deciding which is the best implant for treating each type of fractures. It is consensual that the intramedullary implants have better behaviour than the extramedullary, taking into account the risk of complications [10, 47, 49–51].

Goffin et al. [53] tested a Gamma nail implant and a SHS in both 3-part and 4-part 31-A2 fractures, to assess the behaviour of the two implants, evaluating the von Mises stress on the implant and the minimum principal strains on the bone. Isotropic and homogeneous material properties were used for all materials, including the bone. They concluded that the Gamma nail presented better fixation results than the SHS, according to a lower propensity to yielding observed in the von Mises stress distribution, and that fixation on the more unstable 4-part fracture was harder to achieve even with the better implant. Helwig et al. [62] compared the performance of 4 intramedullary implants, on a femur model with inhomogeneous properties, with the Targon PF implant being the most successful on preventing cut-out. Huang et al. [63] compared the Gamma nail with the DHS for a 31-A2 and a 31-A3 fractures, concluding, by analysing the von Mises stresses on the implants, that the Gamma nail has a mechanical superiority over the DHS. Yuan et al. [64] corroborates the superiority of intramedullary

implants by comparing the PFNA and DHS for three osteoporotic bone fractures of types Evans-Jensen II, III and IV.

2.4.2 Bone damage models

The damage of materials is the progressive physical process by which they break, and damage mechanics is the multiscale study of the mechanisms involved in materials' deterioration when subjected to loading, using mechanical variables [65]. This study starts at the microscale, where microvoids and microcracks start the degradation of the structures. At the mesoscale, the growth of the microcracks and microvoids is studied, corresponding to the crack initiation; the growth of the crack is addressed at the macroscale. The micro- and mesoscale studies resort to damage variables on the mechanics of the continuous domain that are defined at the mesoscale level.

Continuum damage mechanics (CDM) is a branch of damage mechanics that treats the damaged material as macroscopically homogeneous, thus making possible to model the propagation of microdefects, including their effect on the stress-strain behaviour [66]. This theory takes a damage parameter, D , accounting for the microscopic deteriorations (voids, microcracks, etc.) on a microscopic scale, with a lower limit $D = 0$ for the initially unstressed material and an upper limit $D = D_c$ at the material failure, where D_c denotes the critical damage parameter. The effective stress applied to the material is defined in terms of the damage variable as:

$$\bar{\sigma} = \frac{\sigma}{(1 - D)} \quad (2.1)$$

meaning that a damaged volume of material under the applied nominal stress σ shows the same strain response that the undamaged one submitted to the effective stress $\bar{\sigma}$. This means that the stiffness of the material, described by the Young's modulus, is negatively correlated with the damage.

Bone damage models have become increasingly popular in the last years. Below the yielding limit, bone behaves elastically with the same stiffness for both tension and compression. However, because of the bone's particular properties structural properties, material properties like yield stress or strain, strength and fracture strain depend on whether the material is under tensile or compressive conditions. When a bone is loaded past the yielding point, two mechanisms for energy dissipation occur: plasticity and damage. Plasticity is manifested as permanent deformation after unloading, whereas damage is associated with a reduction of stiffness due to the formation of microcracks [29]. Research groups have been developing several models, from simple element-deletion models to more sophisticated fracture energy-based models [29]. Most of these studies' results have been validated with experimental results.

Dapaah et al. [67], Garcia et al. [68], Zysset and Wolfram [69], and Schwiedrzik and Zysset [70] developed damage models using fracture energy concepts. Their damage evolution equations were derived from energy and dissipation potentials. Some authors developed quasi-brittle damage models, using stress-strain relations based on Hooke's law and experimental data to adjust the damage evolution functions [71–73]. Quasi-brittle models are characterized by presenting damage evolution between yield and fracture. Regarding the number of damage variables, some authors used only one damage

variable [70–75], while other authors distinguished between tensile and compressive damage by using two separate variables [67–69].

One of the major differences between the different models is the yield criterion used. Dapaah et al. [67] used the stress-based Hashin failure criteria to define 4 failure modes (the different combinations of longitudinal or transverse, tension or compression). Ng et al. [72] defined a tri-axial stress-based yield criterion, including also a hardening behaviour component. On the other hand, Haider et al. [71] and Hambli et al. [73] used yield criteria based on strain - while Hambli et al. used two yield strain values, one for tension and another for compression, Haider et al. defined yielding based on strain invariants.

Some of these studies were developed for all types of bone tissues [68–70], with some of them even defining different model parameters for trabecular and cortical bone [73]. Haider et al. [71] and Ovesy et al. [75] models were developed for trabecular bone, while Dapaah et al. [67] and Ng et al. [72] models were employed on cortical bone tissues.

Table 2.1 summarizes the features of several experimentally validated bone damage models available in the literature.

Table 2.1: Summary of the characteristics of some damage models present in the literature.

Reference	Yield criterion	Number of damage variables	Energy or stress strain based	Type of bone tissue
[67]	Hashin failure criteria (stress)	2	Energy	Cortical
[68]	Stress	2	Energy	All types
[69]	–	2	Energy	All types
[70]	Stress	1	Energy	All types
[71]	Strain	1	Stress-strain	Trabecular
[72]	Stress with hardening	1	Stress-strain	Cortical
[73, 76, 77]	Strain	1	Stress-strain	All types
[75]	Strain	1	Stress-strain	Trabecular

2.5 Novel aspects of the work

This work advances the studies of Vasconcelos [78] and Quental et al. [19], which assessed the relationship between the risk of cut-out and the blade position using single-iteration FE analyses for both a male and a female femora with PFNA implants, by applying a damage model with stiffness variation to the system, and modelling a more unstable fracture.

To the author’s knowledge, this is the first study to apply a damage model to a bone-implant system of a hip fracture. This work is closer to the real case than the ones by Vasconcelos and Quental et al., since bone stiffness is constantly being adapted according to the damage distribution. The damage distribution also allows identification of the most critical areas on the bone, instead of classifying each point only as damaged or undamaged. Finally, this damage model considers yielding and fracture for

both tension and compression, while the previous studies only consider damage for compressive strains.

Furthermore, the inclusion of different strategies for applying the loads to the system provide information on how damage evolves during gait, providing more accurate information about the most critical regions on the femur, and the analyses with loading above the normal scheme give relevant information about the influence of excessive loads on the damage distribution and the risk of cut-out.

Chapter 3

Methods

This chapter describes in detail the damage model used in this work, the development of the finite element models of the bone and implant, and the coupling of both damage and finite element models. The methodology followed to analyse the results is also presented.

3.1 Damage Model

A quasi-brittle damage model based on continuum damage mechanics was used in this work. This model uses an isotropic behaviour law coupled to a quasi-brittle damage law to describe the damage evolution on the bone and its influence on the structural stiffness reduction. The model is based on a work by Hambli [76]. A damage variable D is defined, which acts as a stiffness reduction factor: its value ranges between 0 (no damage, no loss of stiffness) and 1 (total damage, total loss of stiffness). Considering the damage value, the effective Young's modulus is given by:

$$E = (1 - D) E_0 \quad (3.1)$$

where E_0 is the Young's modulus of the undamaged material, and E is the effective Young's modulus.

Experimental studies [79–81] show that damage accumulation in both trabecular and cortical bones correlates positively with strain above the yield strain, and evolves according to a power law relation. Hambli and Allaoui [77] proposed a quasi-brittle damage evolution law based on continuum damage mechanics theory that is expressed in the following form:

$$D = \begin{cases} 0 & ; \varepsilon_{eq} \leq \varepsilon_0 \\ D_c \left(\frac{\varepsilon_{eq}}{\varepsilon_f} \right)^n & ; \varepsilon_0 < \varepsilon_{eq} < \varepsilon_f \\ D_c & ; \varepsilon_{eq} \geq \varepsilon_f \end{cases} \quad (3.2)$$

where D_c , n , ε_0 and ε_f are respectively the critical damage at fracture (damage threshold above which all stiffness is considered to be lost), the damage exponent, the yield strain (strain threshold when damage starts) and the strain at fracture, and ε_{eq} is the equivalent strain, given by:

$$\varepsilon_{eq} = \sqrt{\frac{2}{3} \varepsilon_{ij} \varepsilon_{ij}} \quad (3.3)$$

This model assumes that the growth of the damage variable is controlled by a function depending on the strain evolution history [73]. This function is defined as:

$$f(\varepsilon_{eq}, \varepsilon_0) = \varepsilon_{eq} - \max(k, \varepsilon_0) \quad (3.4)$$

where k is defined as the maximum equivalent strain reached during loading history, i.e.,

$$k = \max(\varepsilon_{eq}) \quad (3.5)$$

If function $f \geq 0$, damage grows according with equation 3.2; otherwise, damage remains the same. In other words, this means that the value of D cannot decrease.

This damage model handles differently tension and compression. The differentiation is based on whether the hydrostatic stress, σ_H , is positive (tension) or negative (compression). The values of the model parameters (ε_0 , ε_f and D_c) are different for both cases.

The different parameters used on the damage model were obtained from experimental works. Their values and respective sources are detailed in Table 3.1.

Table 3.1: Damage model parameters.

	n	<i>Tension</i>			<i>Compression</i>		
		D_c^T	ε_0^T	ε_f^T	D_c^C	ε_0^C	ε_f^C
Value	2	0.95	0.7%	2.5%	0.5	1.04%	4.0%
Source	[82]	[76]	[83]	[76]	[76]	[83]	[76]

The value of the damage law exponent, n , was based on experimental results by Wolfram et al. [82]. The values of the critical damage threshold for both tension and compression were extrapolated from fatigue loading studies; the approach is that, when the damage parameter reaches its critical value, the evolution is unstable until failure, so failure is considered at that point. The yield and fracture strains were also obtained experimentally.

3.2 Finite Element Model

Three-dimensional geometric models of a male and a female right femora and a PFNA implant, provided by Quental et al. [19], were used as the basis for this work.

The femora models were developed based on sets of medical Computed Tomography (CT) images of a 59 year-old woman and a 38 year-old man. For the sake of brevity, only the modelling of the female bone is described, since the modelling process for the male bone is similar. From these images, based on the intensity of each pixel, the geometry of the bone was obtained by image segmentation, using the software ITK-SNAP (version 3.8.0, 2019). After a bone surface mesh smoothing, performed by the

software MeshLab using a smoothing filter, the 3D surface mesh obtained was exported as a point cloud data file to Solidworks (2020 version) in order to generate a 3D solid model. The 3D models of the femora are presented in Figure 3.1.

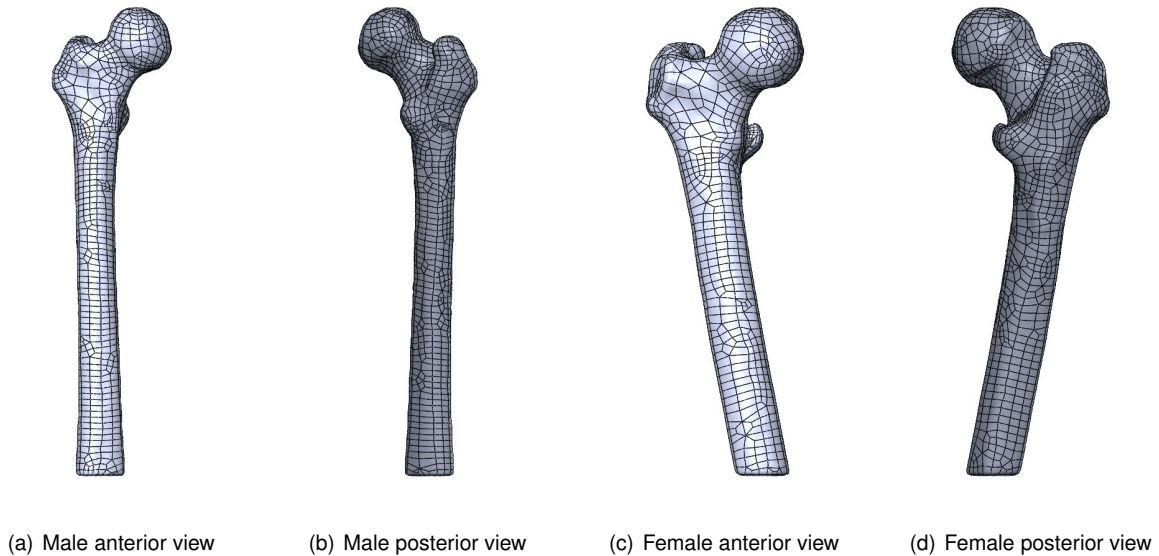


Figure 3.1: Three-dimensional geometric models of a male and a female right femora.

Having the bone model, the trochanteric fracture was modelled. A fracture classified as 31-A2.2 in the Müller AO classification system (cf. fig. 2.9) was modelled from an anteroposterior view, with an angle of 43° between the fracture line and the femoral shaft axis [84], an intrusion distance of 95% of the fracture line length (representative of a 31-A2.2 fracture based on clinical guidance from Dr. Francisco Guerra Pinto, from Sant'Ana Orthopaedic Hospital), and an opening angle of 6.5° . The fracture was modelled using Solidworks *Extruded cut*. The trochanteric fracture is represented in Figure 3.2. The fracture divided the bone model into 2 parts: a superior part (SP), including the femoral neck and head, and an inferior part (IP), including the femoral shaft. The fracture fragments were not included in the model.

The PFNA implant was also modelled in Solidworks. The geometry and dimensions were based on the implant developed by DePuy Synthes. It consists of 3 parts: the nail, which is inserted in the medullary cavity of the femoral shaft; the blade, implanted in the femoral neck and head; and the locking screw, used to lock the distal part of the nail. Figure 3.3 shows the geometry of a real implant and the assembled model of the PFNA developed in Solidworks.

Finally, all components were assembled. The implant was inserted into the bone following the guidelines of the surgical technique guide provided by DePuy Synthes [20]. The two parts of the bone were initially placed on their original position before fracture. The entry point for the PFNA was defined as the tip of the greater trochanter, in line with the axis of the medullary cavity in the lateral view, and the entry orientation was chosen to create an angle of 6° with the femoral shaft in the anteroposterior view. A hole with a 16.5 mm diameter was opened from this point to the region above the lesser trochanter, using once again the feature *Extruded cut* from Solidworks. Afterwards, a hole with an 11.5 diameter

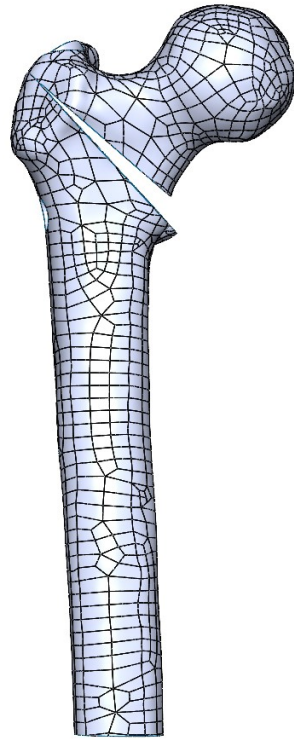


Figure 3.2: Geometric model of a female femur with a 31-A2.2 fracture.

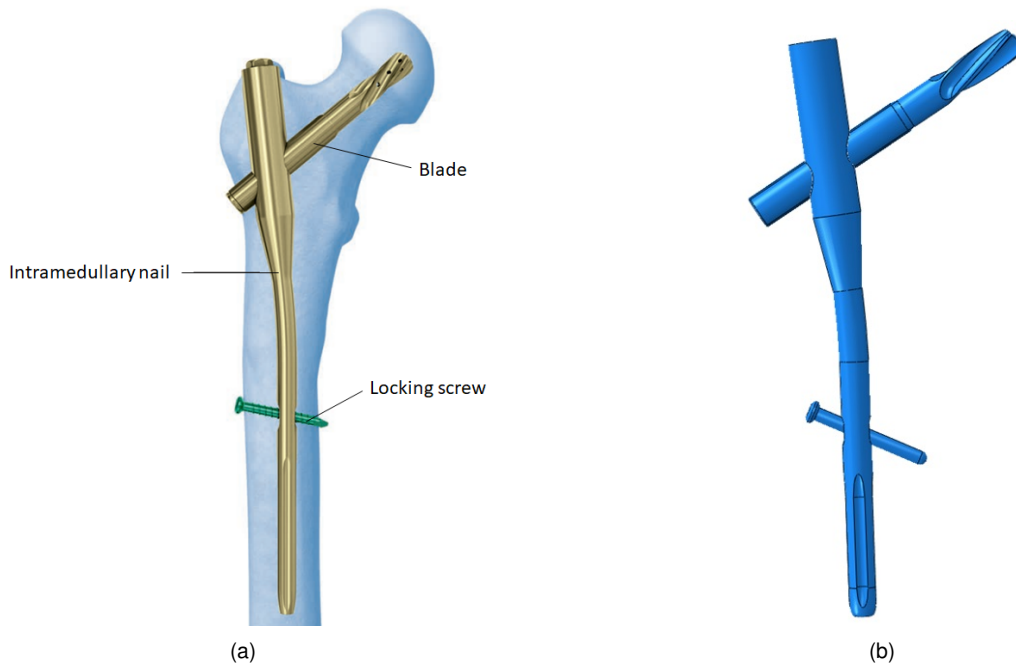


Figure 3.3: (a) Geometry of a real PFNA implant [20] and (b) 3D geometric model developed in Solid-works.

was created in the medullary cavity. The PFNA nail was then inserted through this hole.

After the insertion of the nail, the blade was positioned aligned with the femoral head centre in the lateral view, through the bone surface in the lateral direction, and with different distances from the femoral head external surface, depending on which medial-lateral position for the blade would be used on the model - distances of 5 mm, 10 mm, 15 mm and 20 mm to the external femoral head surface were used

for both the central and inferior positions on the anteroposterior view. Henceforth, and for the sake of simplicity, each geometry is referred to by a code starting with the letter M or F (whether the model is of the male or female femur, respectively), followed by "inf" for central-inferior positions and "cent" for central-central positions, and by the distance, in millimetres, from the tip of the blade to the external surface of the femoral head (e.g. Minf5, Fcent20). After positioning the blade, Solidworks' feature *Cavity* was employed to create a hole in the bone with the geometry of the blade. Figure 3.4 shows the 8 assembly configurations modelled for the female bone.

The last part to insert in the assembly was the distal locking screw. The static distal locking strategy was chosen. A diagonal hole was opened for the screw to be inserted, fixing the distal end of the nail and blocking its movement.

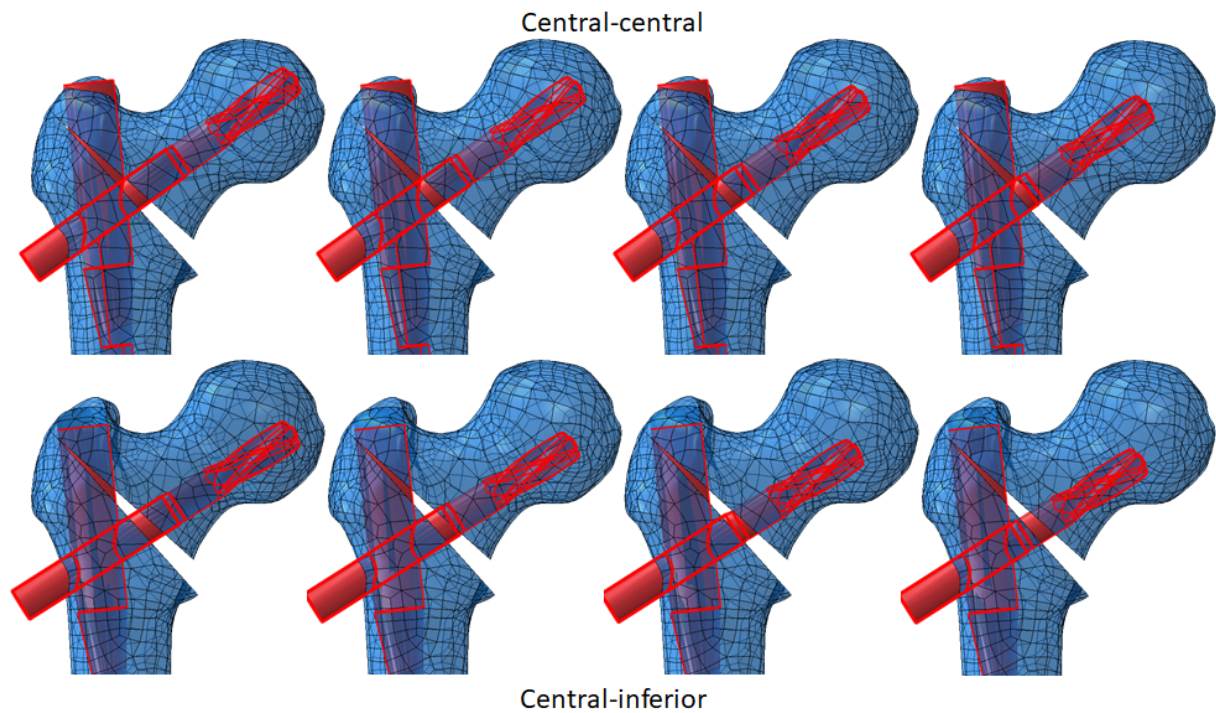


Figure 3.4: Representation of the eight configurations of the implant on the female bone. From left to right: distances of 5 mm, 10 mm, 15 mm and 20 mm from the tip of the blade to the external surface of the femoral head.

The material properties were then assigned to the parts in Abaqus (2017 version). The implant is made of a titanium alloy (Ti-6Al-7Nb), with a Young's modulus $E = 105$ GPa and a Poisson's ratio $\nu = 0.3$. The bone material was modelled as a linear elastic isotropic material, with its Young's modulus depending on bone density, as suggested by several authors [85]. In order to define the density distribution of the bone model, the first step was to obtain the CT gray value from the intensity of each pixel from the CT images. These values were obtained using an Abaqus plug-in called Bonemapy, on a scale called the Hounsfield Units (HU). This scale compares the attenuation coefficient of each point in the material with that of water. Afterwards, this set of HU values was converted to apparent densities, using a calibration law that interpolates the HU values between a maximum (1.86 g cm^{-3}) and a minimum (0.01 g cm^{-3})

density, which are typical values for healthy bones. Afterwards, and since these models correspond to a 59 year-old woman and a 38 year-old man, but hip fractures happen more frequently and are more critical in the elderly population, the bone densities were reduced by 29% to simulate the poorer conditions of an elderly bone [19, 86]. The maximum density was reduced to 1.32 g cm^{-3} . Figure 3.5 shows the distribution of densities for the female bone model.

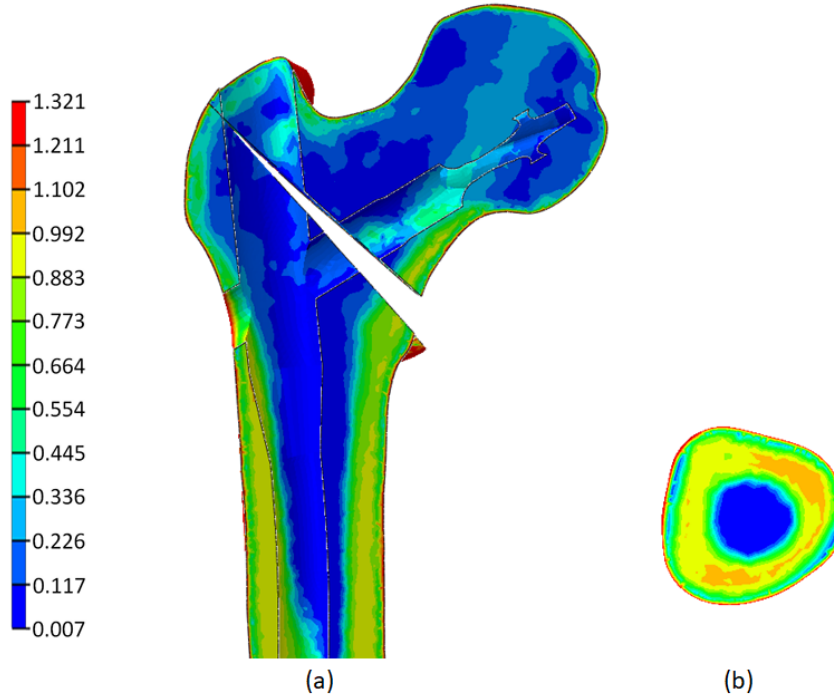


Figure 3.5: Density distribution, in g cm^{-3} , on the osteoporotic female proximal femur model. (a) Anteroposterior view of a coronal cut; (b) Superior view of a transversal cut.

Because of the finite spatial resolution of the imaging device, a single voxel may contain several types of tissues, especially at tissue interfaces, complicating the segmentation process. This is called the partial volume effect [87, 88]. In order to avoid inaccuracy on the model resulting from this problem, and to ensure that the outer surface of the bone represents cortical bone, the maximum value of the density was assigned to all superficial nodes. Also, two additional structures were modelled - for each part of the bone, a shell corresponding to its external surface was obtained using an Abaqus feature that automatically generates shell structures from solids. These shells represent the external cortex of the bone, and were assigned a Young's modulus of 10.37 GPa, corresponding to the Young's modulus of the maximum bone density considered, and a thickness of 0.5 mm [89, 90]. The shells are displayed on Figure 3.6

An in-house MATLAB program was used to map the densities and convert the density distribution from the intact model to the fractured one. For each node on the new model, this program defined its density: (i) equal to the density of a node on the original model, if the coordinates of both nodes were the same, or (ii) as a weighted average, with the inverse of the square of the distance, of the nodes on the original model with the closest coordinates.

Different laws relating Young's modulus and bone density are available in the literature [85]. Schileo

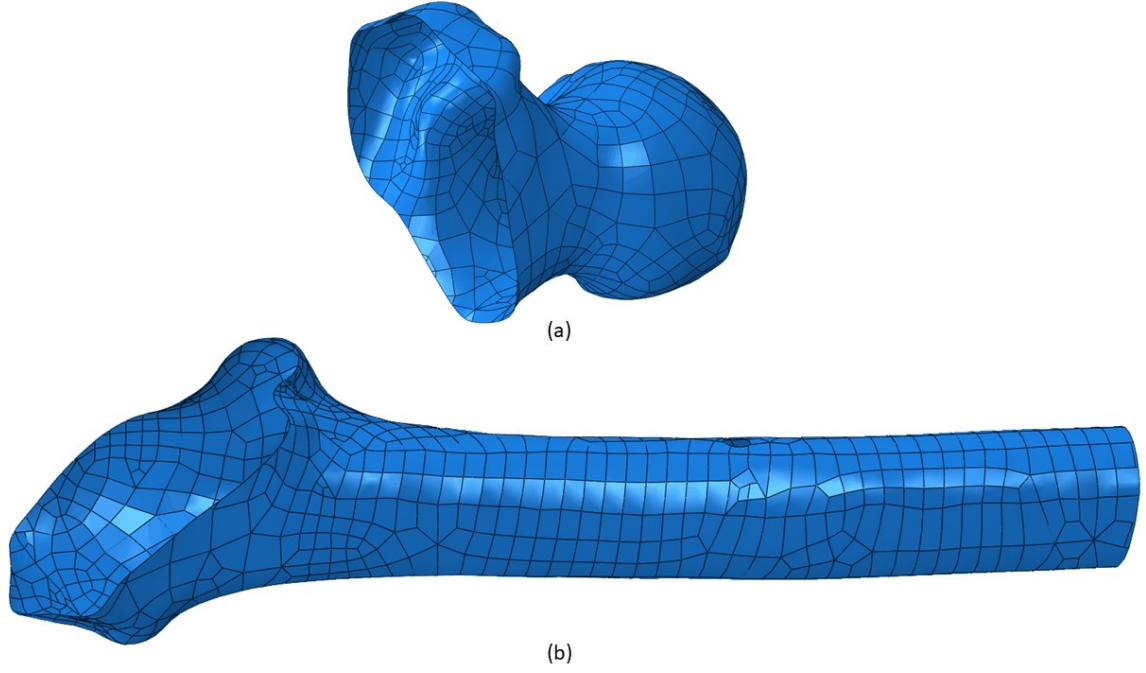


Figure 3.6: Shells simulating external cortical bone of the femur: (a) SP and (b) IP.

et al. [91] performed a comparative study between a selected set of laws, concluding that the model by Morgan et al. [92] performs better comparing to experimental results, which led to the selection of this model for the present work. The relationship between Young's modulus and the apparent density in each point is then given by:

$$E_0 = 6850 \rho^{1.49} \quad (3.6)$$

where ρ is the apparent density in each point of the bone. This law leads to a Young's modulus ranging from 4.31 MPa on the lowest density points to 10.37 GPa on the densest zones.

The interactions defined in Abaqus between parts were of two types: tie constraints and surface-to-surface contact interactions. The outer cortical bone shells were tied to the bone. A tie constraint was also defined between the distal locking screw and the bone. Despite not being representative of the real contact, this approximation was made for the sake of simplicity, since this contact is expected to have little impact on the results.

The other interactions were defined as surface-to-surface contact. There are 3 types of surface interactions: bone-bone, bone-implant, and implant-implant. The bone-bone interaction between the superior and inferior parts of the bone considered a friction coefficient of 0.46 [7]. The interactions between the bone and the nail and between the bone and the blade considered a friction coefficient of 0.3 [7]. Finally, the implant-implant interactions, defined between the nail and both the blade and the locking screw, had a friction coefficient of 0.2 [93].

The loading conditions were defined to simulate the forces acting on the femur during gait. According to Heller et al. [32], the forces on the proximal femur during walking are applied on 3 points, designated

as P_0 , P_1 and P_2 . These points represent, respectively, the hip contact point on the femoral head; the application point of the forces related to the abductor muscles and both the tensor fascia latae, located on the lateral region of the greater trochanter; and a point on the lateral region below the line of the lesser trochanter where the vastus lateralis attaches. The attachment points locations are represented in figure 3.7. All these 3 points were defined in Abaqus as Attachment Points, and were coupled to shell areas on their vicinity using Coupling constraints, so that each applied force was distributed by a number of nodes, avoiding high punctual stresses. The distribution of the force on point P_0 was defined to be quadratic over the slave surface, by defining the coupling type as continuum distributing with a quadratic weighting method, while the forces acting on points P_1 and P_2 were distributed according to a uniform weighting method [89].

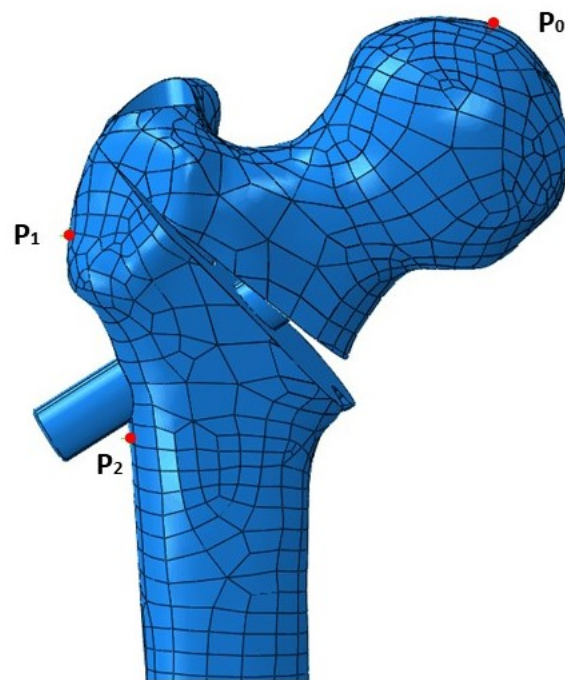


Figure 3.7: Attachment points for the application of loads in the female model.

Heller et al. [32] present the load values as percentages of the bodyweight. Table 3.2 presents the loading conditions for both the male and female bones, already converted to Newton. Columns M and F present their value for the male and female models, respectively. The loads are given in the coordinate system described by Bergmann et al. [94], which aligns its z axis with the femoral shaft axis. Figure 3.8 presents the coordinate system. After the loads were applied, to prevent rigid body motion, the base of the femur was constrained using an encastre condition.

The last step on the finite element model creation was the mesh generation. The 3D solid parts – bone and implant – were discretized using quadratic tetrahedral elements (C3D10). These elements have 10 nodes and 4 integration points, as represented in Figure 3.9. The choice to generate quadratic elements was made due to the complexity of the structures, particularly the bone parts. The bidimensional shell parts were discretized with quadratic triangles (STR165). Mesh sizes were defined following Quental et al. [19], who performed a convergence analysis to select a proper element size for the mesh.

Table 3.2: Loads acting on the proximal femur. M and F are the load values in Newton for the male and female bone, respectively (adapted from [32]). TFL is short for the muscle tensor fascia latae.

	F_x		F_y		F_z		Point
	M	F	M	F	M	F	
Hip contact	481.0	400.0	-292.2	-242.9	-2041.6	-1697.6	P0
Abductor	-516.6	-429.6	38.3	31.8	770.5	640.7	P1
TFL, proximal	-64.1	-53.3	103.3	85.9	117.6	97.8	P1
TFL, distal	4.5	3.7	-6.2	-5.2	-169.2	-140.7	P1
Vastus lateralis	8.0	6.7	164.8	137.0	-827.5	-688.1	P2

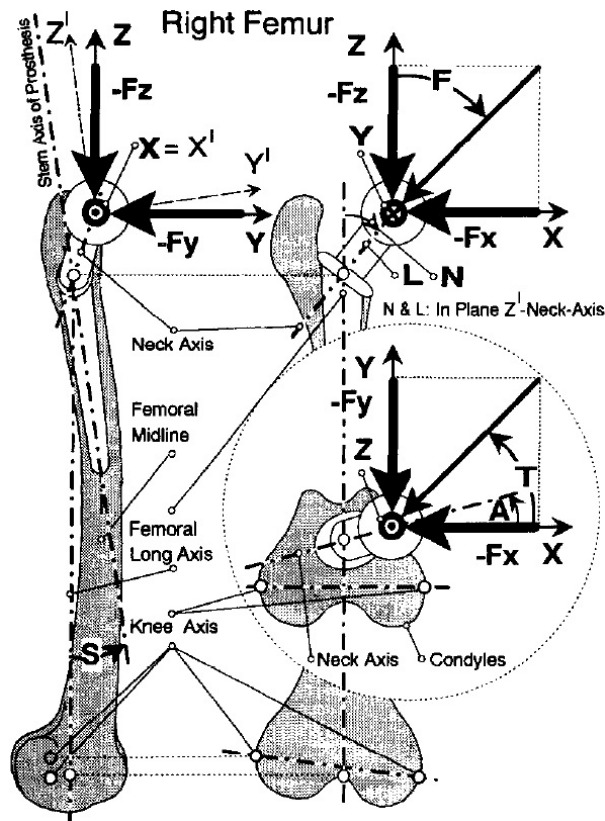


Figure 3.8: Coordinate system used to describe the loading conditions [94].

The convergence was assessed based on the evolution of the minimum principal strain on 3 nodes of the model with the element size. They concluded that the optimal element size to satisfy both convergence and computational efficiency was 2 mm for the SP and 3 mm for the IP and the implant.

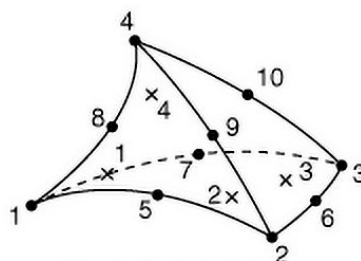


Figure 3.9: Position of nodes and integration points (x) in a C3D10 element [95].

3.3 Damage model and FEM integration

In this work, the FE models described in section 3.2 were coupled with the Damage Model presented in section 3.1. The domain was discretized by the FE model, and the damage model was applied locally to each node of the bone, using the equations in section 3.1. Stresses and strains were computed through FE analyses.

The application of the damage model equations provides a nodal damage distribution for both the SP and IP of the bone. This damage distribution affects the Young's modulus distribution, but only takes effect on a next FE analysis. This requires the implementation of an iterative procedure. Three different load application strategies for the simulations were considered: (i) loads were gradually incremented using loads steps (for example, starting with 25% of load, 25% load increments were applied after each iteration until all load was applied); (ii) full loading was initially applied but several iterations were performed until the damage distribution changed less than a predefined threshold; (iii) loads were gradually incremented, as in (i), and several iterations were performed after reaching full load until damage changed less than a predefined threshold, as in (ii). Henceforth, for the sake of simplicity, strategy (i) is referred to as incremental loading strategy, strategy (ii) as full loading strategy and strategy (iii) as hybrid strategy.

The convergence criterion for the full loading strategy was based on the variation of a parameter internally named DIVol. This parameter is given by

$$\text{DIVol} = \iiint_V D \, dV \quad (3.7)$$

where V is the total bone volume. Discretizing for the finite element method:

$$\text{DIVol} = \sum_{e=1}^{\text{NE}} \iiint_{V^e} D^e \, dV^e \quad (3.8)$$

where NE is the number of elements of the bone mesh. Finally, resorting to Gauss integration:

$$\text{DIVol} = \sum_{e=1}^{\text{NE}} \sum_{i=1}^{\text{NIP}} D_i^e \text{IVol}_i^e \quad (3.9)$$

where NIP is the number of integration points per element, which is 4 for C3D10 elements (cf. Figure 3.9) and IVol is the volume associated to each integration point. To compute this parameter, both the damage and volume data were obtained at the integration points. To interpolate the damage from the nodes to the integration points, the nodal damage data was imported to Abaqus as a field variable. Importing the damage data as field variables, Abaqus automatically interpolates the values from the nodes to the integration points when the FEA is performed, and these data can be extracted along with IVol. DIVol is, then, a measure that combines the volume of bone with damage to the actual damage value on each point.

For each iteration, a convergence parameter (CP) was computed as the relative deviation of DIVol between the current and previous iterations, i.e.,

$$CP = \frac{DIVol - DIVol_{prev}}{DIVol_{prev}} \quad (3.10)$$

The convergence parameter was compared, in each iteration, with a user-defined tolerance to check for convergence - if CP was below the tolerance, the process was considered to have reached convergence.

After each FEA execution, the stress and strain results were used to update the damage distribution on the bone. For the next iteration to take into account the stiffness loss resulting from the damage distribution, the bone material model was adapted to include the stiffness reduction. For the sake of simplicity, a new parameter $\alpha = (1 - D) \rho^{1.49}$ was defined for each node. This allows the nodal effective Young's modulus (cf. equation 3.1) to be rewritten as a linear function:

$$E = 6850 \alpha \quad (3.11)$$

Whenever a node, whether under tension or compression state, reached the respective critical damage threshold, its damage value was set to 1, such that (i) the visualization of the critical damage areas became clearer and (ii) the value of α was automatically set to 0. According to the material equation, a node with a null α would have a null Young's modulus. However, as a way of avoiding numerical instabilities, a low Young's modulus of 0.01 MPa was considered [62]. In some cases, the minimum stiffness was too small, causing convergence problems. To overcome these convergence problems, the minimum stiffness was updated to 0.1 MPa whenever convergence problems arose. To make sure that this procedure had little impact on the results, a sensitivity analysis was performed, as shown in the Appendix A.

A MATLAB code was developed to implement the algorithm as represented in Figure 3.10. It starts by reading the loads, nodal densities and model parameters (cf. table 3.1), along with data for the algorithm, namely the convergence tolerance for the full loading strategy and the number of steps for the incremental loading strategy. The initial file with the nodal α values is written. Afterwards, if the incremental loading strategy is to be performed, a *for* cycle, with the previously defined number of steps, is initiated. This cycle starts by incrementing the loads for the new load step. The FEA is performed and the results necessary for the damage model - stresses and strains - are extracted. The damage model is applied to each node of the bone, and the resulting nodal damage and α are written to files. This repeats until the number of iterations performed matches the number of load steps previously defined.

The full loading strategy, that can occur after the incremental loading (for the hybrid strategy) or independently, starts by defining the full 100% loading and writing it to the loads file. The next steps are similar to the ones happening on the incremental loading strategy, from running the FEA to writing the damage and α files.

At the end of each iteration, parameter DIVol and the convergence parameter are computed. The cycle starting on the FEA execution is repeated until the convergence parameter is below the tolerance previously defined.

The damage model algorithm implemented as a MATLAB function is shown in Figure 3.11. The

same algorithm runs for each node of both SP and IP of the bone, to obtain the damage distribution on all nodes. It starts by computing the hydrostatic stress using the relation

$$\sigma_H = \frac{\sigma_{xx} + \sigma_{yy} + \sigma_{zz}}{3} \quad (3.12)$$

with the stress information obtained from the FEA. It also computes the equivalent strain using expression 3.3. Then, the program checks whether the node is under tension or compression conditions, by checking the hydrostatic stress sign. If the node is under tension, the damage parameter is computed using tension parameters and the algorithm moves on. On the other hand, if the node is under compression, the program checks its previous state. If it was already under compression, the damage parameter is normally computed using compression parameters and the algorithm moves on; otherwise, the critical damage parameter decreases, implying that, if the damage parameter in a node was already above the compressive critical damage, that node becomes critically damaged. The damage parameter in the non-critically damaged nodes is computed as usual.

From equation 3.4, the damage value can only remain constant or increase. To ensure this condition, an equivalent approach was implemented: the program checks the relationship between the damage of the node and the damage of the same node on the previous iteration, and if the newly computed damage is smaller than the previous one, its value is redefined as the previous one.

Finally, the function verifies if the node has reached critical damage - if so, its damage value is set to 1. The same cycle runs until all nodes have been evaluated.

3.4 Analysis of results

In this section, the methods used for the analysis of the results are presented. It starts by describing the methods used for the verification of the damage model implemented. Afterwards, the methods for assessing the risk of cut-out in all models are explained.

3.4.1 Methods for damage model verification

Quental et al. [19] assumed a relationship between high compressive strains and the risk of cut-out. They evaluated the risk of cut-out by computing the volume of bone with minimum (compressive) principal strains that exceeded a yield strain of -0.84%. In order to verify the damage model implemented in this work, the damage distribution results of a female model were compared with the results obtained for the same model with the methodology used by Quental et al.. To be coherent, only the compressive damage obtained from the damage model was considered, with the tensile damage elements being ignored for purposes of this comparison.

3.4.2 Analysis of the risk of cut-out

Several authors have assumed a relation between the volume of yielded bone and the risk of cut-out [18, 19, 53, 78]. Goffin et al. [18] evaluated only the superior part of the bone (SP), stating that cut-out is likely to occur due to high compressive strains in the whole head and neck regions. In order to take advantage of having a damage model differentiating the damage intensity, a new parameter was developed to evaluate the risk of cut-out. This parameter, named DIVol-SP, was computed like DIVol (cf. Equation 3.9), but only included the superior part of the bone. DIVol-SP works like a weighted volume that allows for nodes with higher damage to be considered more than those with a lower damage value.

To evaluate the influence of the superior-inferior and medial-lateral positions of the blade, simulations were performed for the eight configurations presented in figure 3.4, for both the female and male models.

The influence of higher loading conditions in the damage evolution, intending to represent incidents, was also investigated. Simulations with double the loads proposed by Heller et al. [32] were performed. Because of limited computational capacity, it was not possible to perform simulations for all models; therefore, models Finf5 and Fcent20 were chosen, since they represent, according to Quental et al. [19], the safest and least safe positions of the female model.

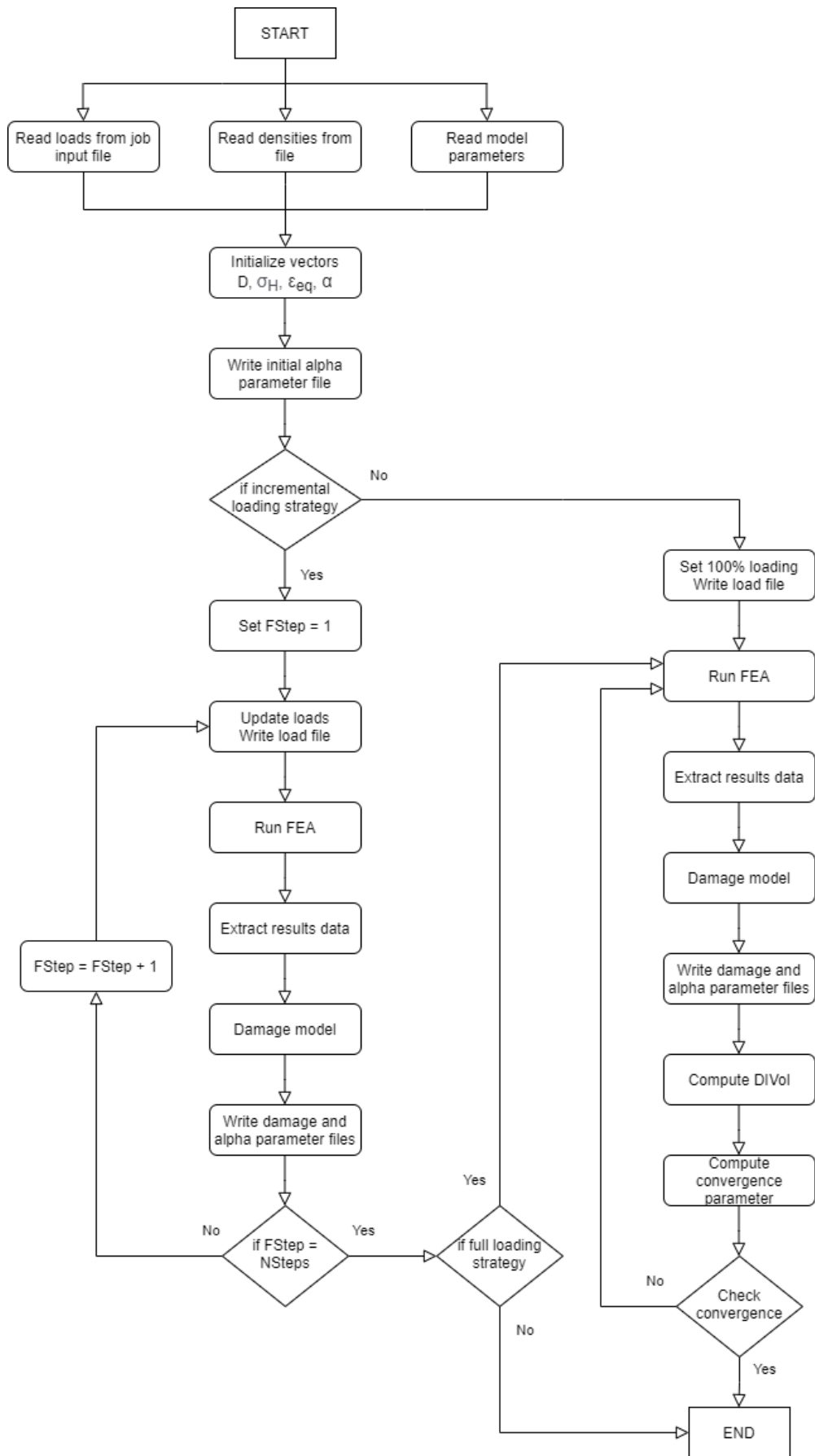


Figure 3.10: Schematic of the algorithm implemented in MATLAB.

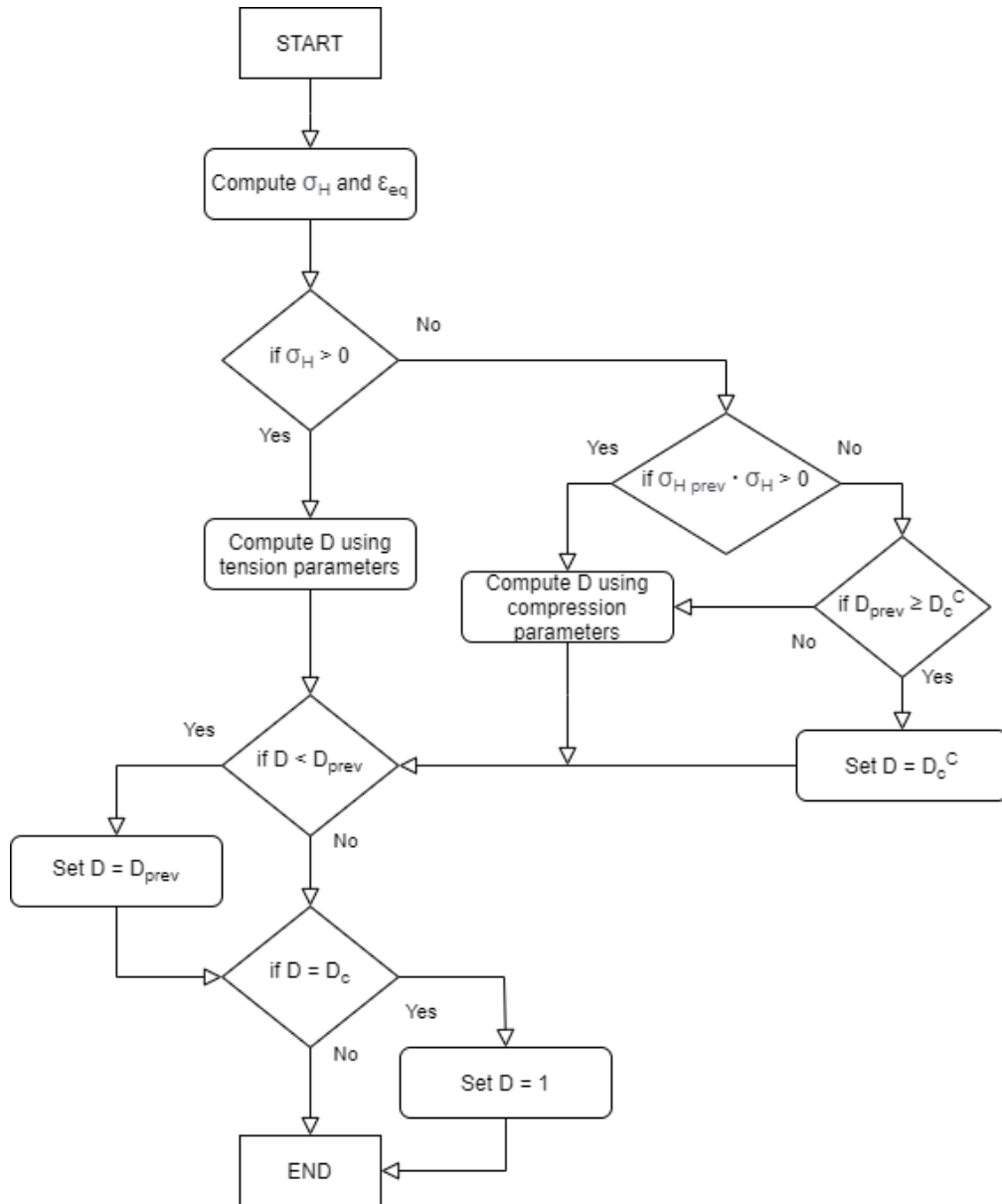


Figure 3.11: Schematic of the damage model algorithm implemented in MATLAB.

Chapter 4

Results

In this chapter, the results obtained in this work are presented. After a verification of the damage model behaviour, the results used to choose between the three load application strategies are presented and discussed. Finally, both the visual and numerical results of the several bone models developed are introduced.

4.1 Damage model verification

To gain confidence on the damage model behaviour, the results obtained were initially compared with those of Quental et al. [19]. A qualitative comparison was made by visually inspecting the damage distribution now obtained and the minimum principal strain distributions in Quental et al., since this study considered damage to occur where the minimum principal strain exceeded a compressive yield strain of -0.84% . Figure 4.1 depicts, from an anteroposterior view on a coronal section, the minimum principal strain and the compressive damage distribution in the Finf5 model.

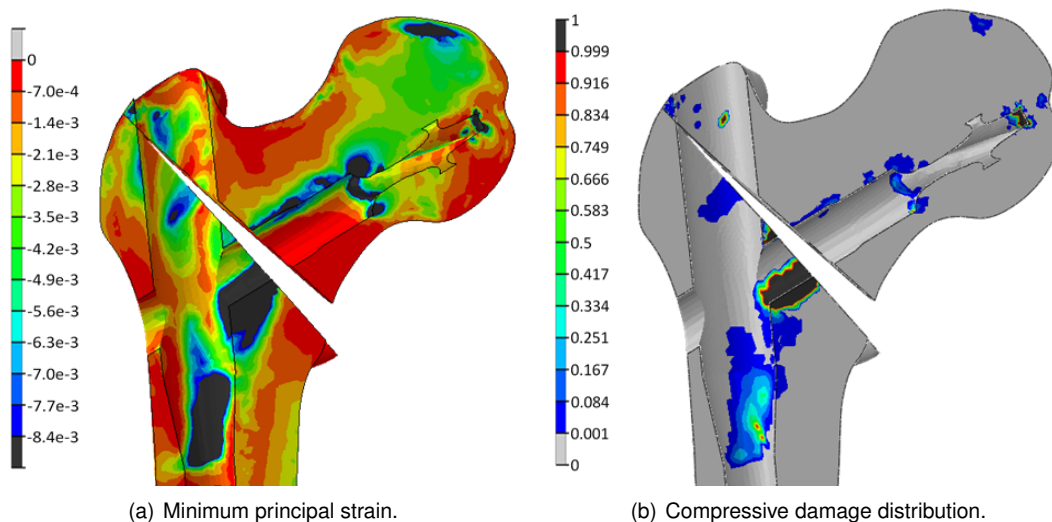


Figure 4.1: Comparison between the damage distribution on the Finf5 model, using (a) minimum compressive principal strains higher than -0.84% as yielding criterion and (b) the damage model implemented.

The damaged zones distribution in both figures are similar, providing confidence in the correct implementation of the damage model used. Although residual differences exist on the distribution of damage from both models, the different yielding criteria used may explain this.

4.2 Loading strategies evaluation

As mentioned in Section 3.3, three possible strategies were identified for load application. In the present section, the three strategies are compared, with the aim of choosing the best one to implement in this work.

The incremental loading strategy was tested resorting to the Fcent20 model. Figure 4.2 presents the evolution of parameter DIVol with the percentage of the total load applied for different number of steps – 4, 6, 8 and 16 – and Figure 4.3 depicts the damage distribution resulting from each one of these analyses. No higher numbers of steps were used due to the high computational cost – the analysis with 16 steps took 4.5 days to conclude. Two main conclusions may be drawn from these results: the final value of DIVol and, consequently, the damage distribution, depend substantially on the number of steps; and, although visually the solutions with 8 and 16 steps have similarities, there are no signs of convergence between 4 and 16 steps when evaluating DIVol. This strategy was therefore excluded.

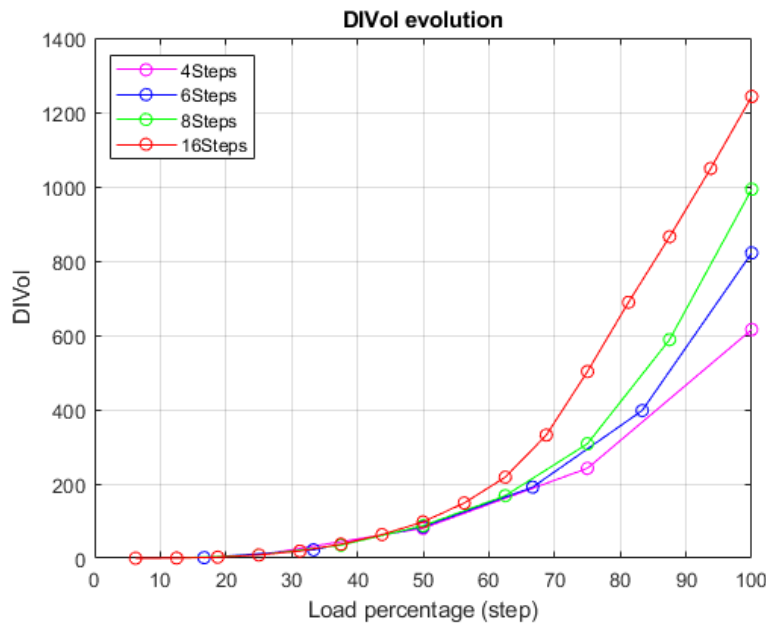


Figure 4.2: DIVol evolution on the Fcent20 model for different numbers of steps.

To decide between the full loading and the hybrid strategies, the two were tested for both a female and a male models. The number of steps was set to 4, a reasonable number taking into account computational efficiency, and the tolerance parameter for the convergence parameter (cf. equation 3.10) was set to 5%. Table 4.1 presents the DIVol evolution over the number of iterations, along with the final deviation between the results from both strategies and the computational time for each of them. Figure 4.4 present the final damage distribution for these female and male simulations, respectively. For the

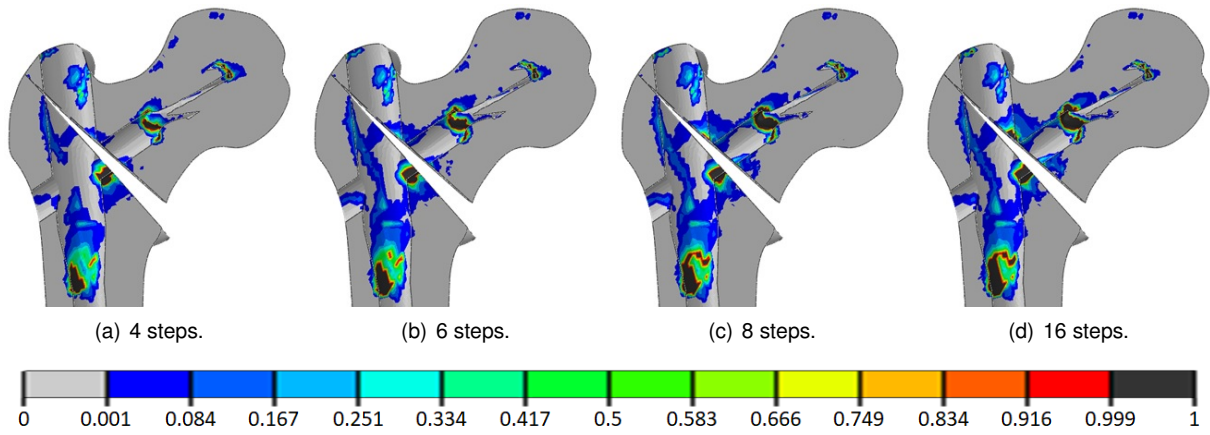


Figure 4.3: Comparison between the final damage distribution on the Finf20 model, for different numbers of load steps.

female model, the evolution of the damage distribution with the increment of load is also displayed, in Figure 4.5. The evolution of DIVol with the number of iterations for the female model is shown in Figure 4.6.

Table 4.1: DIVol evolution with iterations at full loading for the Minf5 and Finf10 models. FLS stands for full loading strategy, and HS for hybrid strategy.

Iteration number	1	2	3	4	5	6	7	Final deviation	Time [h]
Minf5 FLS	999.40	1678.91	2055.33	2289.03	2524.32	2666.20	2765.01	5.4%	110
Minf5 HS	1419.14	1826.76	2111.15	2304.17	2502.89	2615.77			127
Finf10 FLS	331.08	527.83	656.58	734.19	798.57	836.18		5.2%	47
Finf10 HS	452.79	607.08	724.93	804.03	854.00	882.00			54

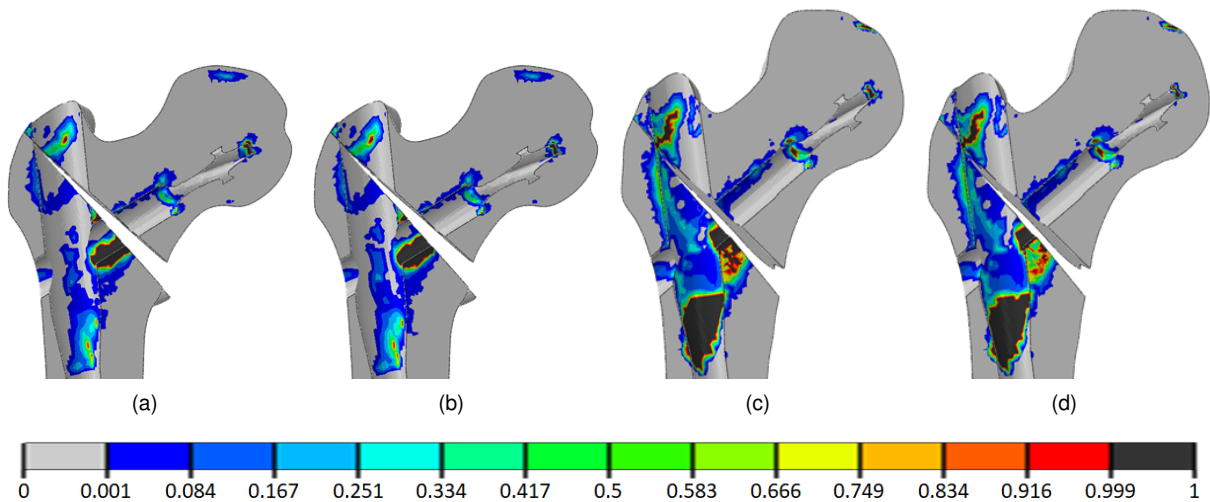


Figure 4.4: Damage distribution on the Finf10 and Minf5 models for both the full loading (FL) and the hybrid (H) load application strategies. (a) Finf10 FL; (b) Finf10 H; (c) Minf5 FL; (d) Minf5 H.

Visually, the damage distributions are similar for both the female and male models. The deviation between the DIVol parameter obtained from both strategies decreases with iterations and stabilizes

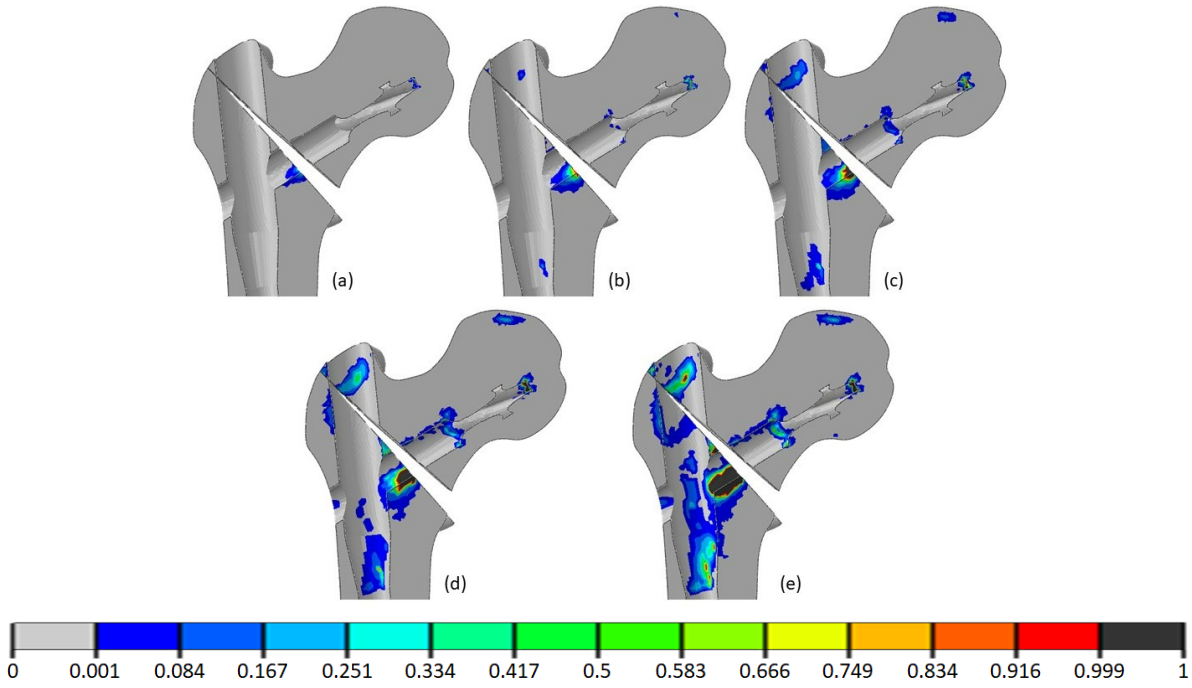


Figure 4.5: Damage distribution on the Finf10 model, for (a) 25% loading, (b) 50% loading, (c) 75% loading and (d) full loading. The final result after several iterations with full loading is shown in (e).

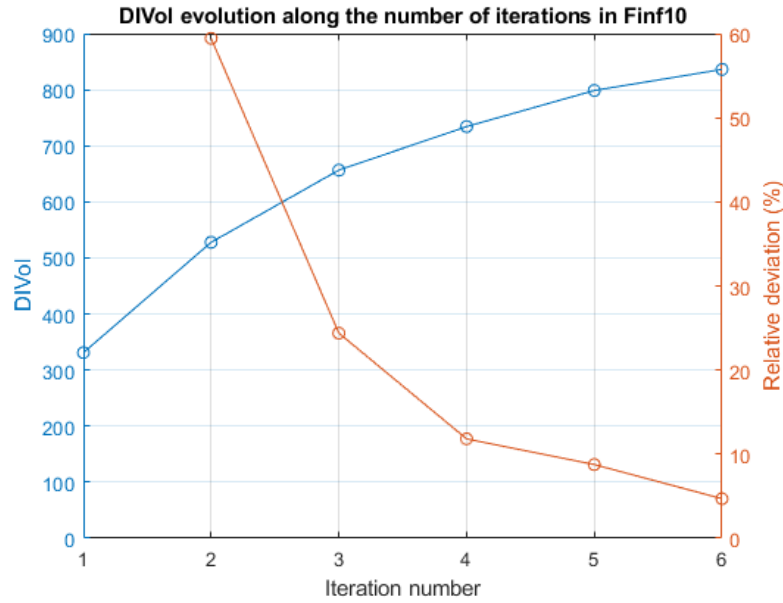


Figure 4.6: DIVol evolution along the number of iterations in Finf10 using the full loading strategy.

around 5% when convergence is reached. Since the damage distribution is stabilized, and the deviation between the final DIVol is approximately the same as the tolerance for convergence, both strategies seem to be converging to the same final result. Considering that, for this work, only the final damage distribution is relevant, the selection of the loading strategy was based on the computational efficiency. Table 4.1 shows that the full loading strategy is more efficient, since the computational time was lower for both the female and male models. Therefore, this strategy was chosen and used in the simulations presented in this chapter.

4.3 Assessment of the risk of cut-out

In this section, the results of the simulations performed for assessing the risk of cut-out are presented.

4.3.1 Damage distribution

Figures 4.7 and 4.8 present the damage distribution resulting from the gait load case for all geometries of, respectively, the female and male models. In both central-central and central-inferior positions, three main regions tended to be critical: at the tip of the blade; around the region where the blade transitions from a cylindrical shape to a helical shape; and at the contact regions immediately above and below the fracture. Also, comparing the positions along the medial-lateral directions, damage increased with the distance to the femoral head surface in the three regions.

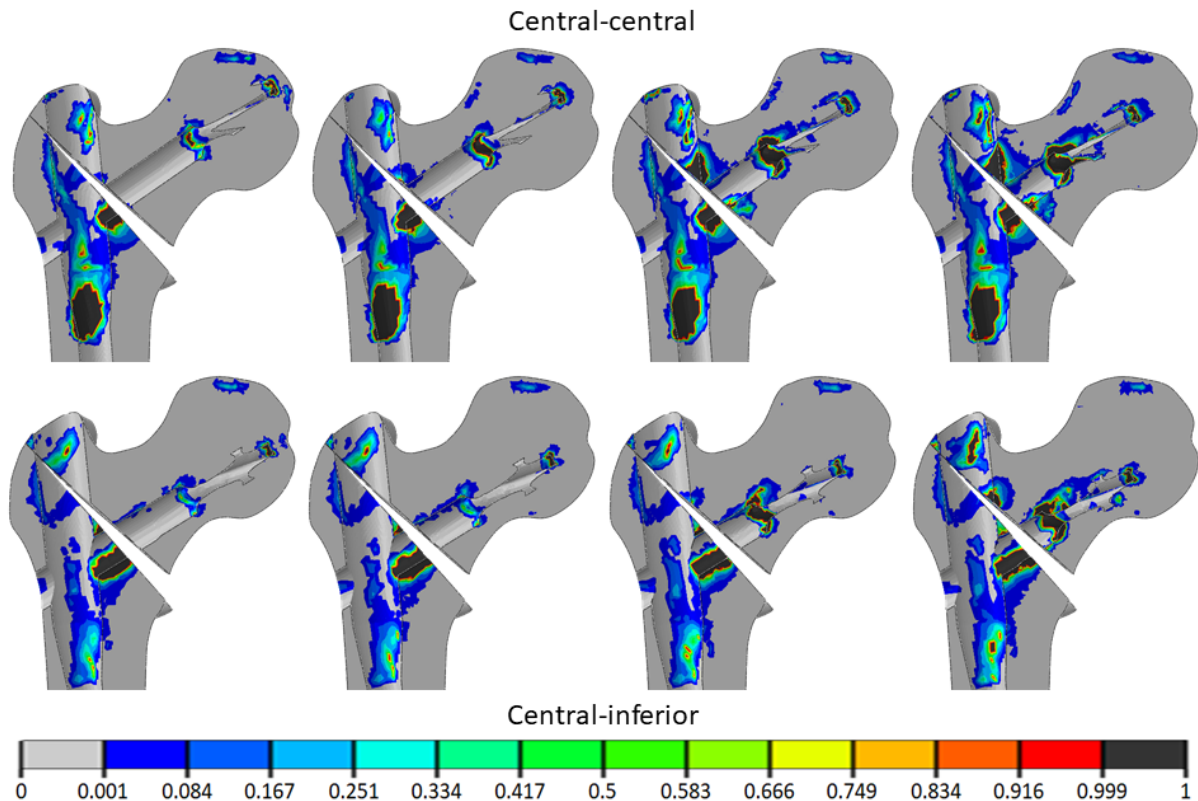


Figure 4.7: Damage distribution on the female bone models. From left to right, distances from the tip of the blade to the femoral head surface of 5, 10, 15 and 20 mm.

Figure 4.9 presents the DIVol for both the SP and IP of all geometries for both the female and male models, for qualitative comparison of the bone damage.

4.3.2 Overload effect

The effect of a loading intensity above normal was also evaluated. The upper line in Figure 4.10 presents the damage distribution for the Finf5 model with the normal loading scheme and with a 100%

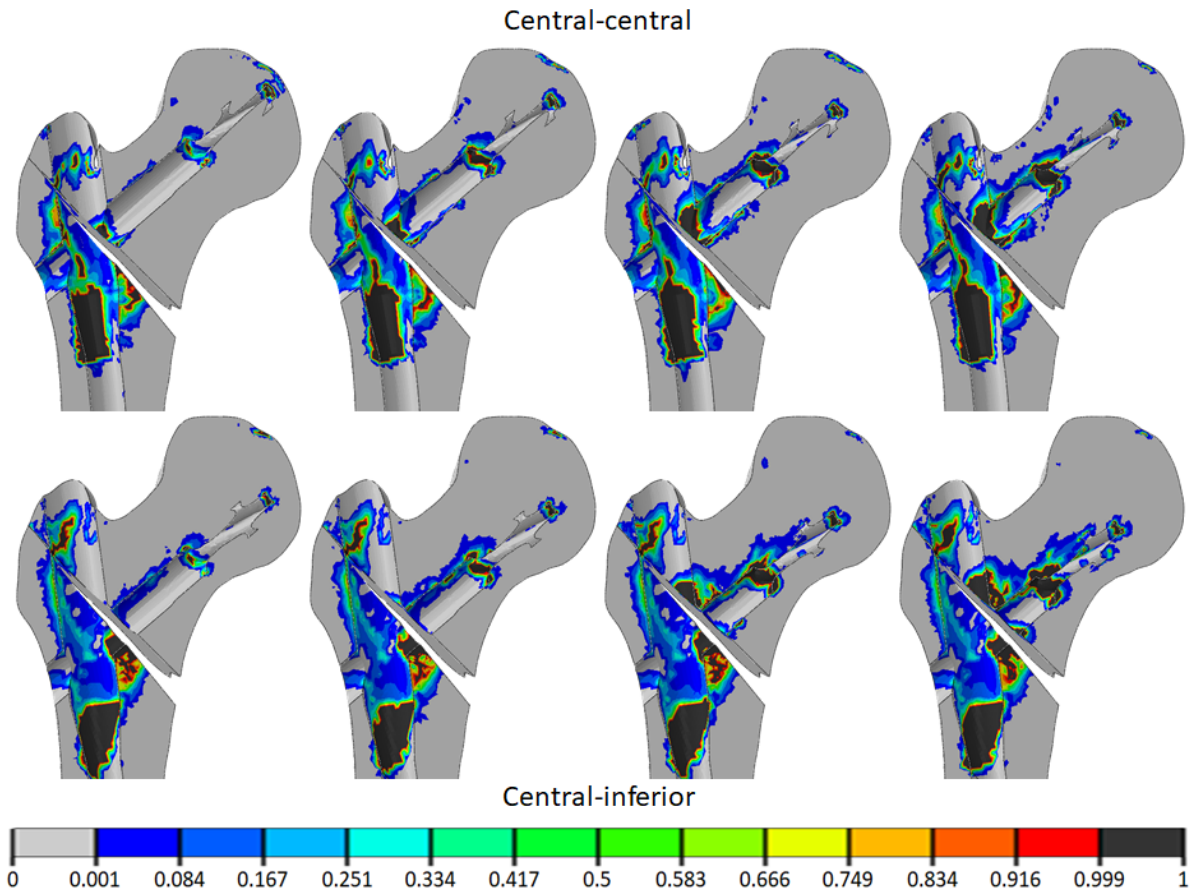
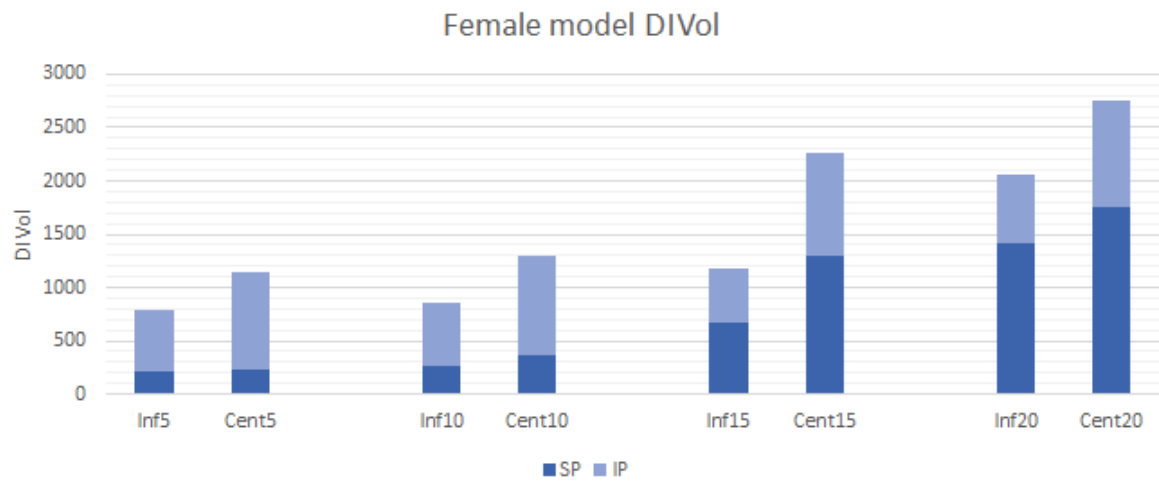


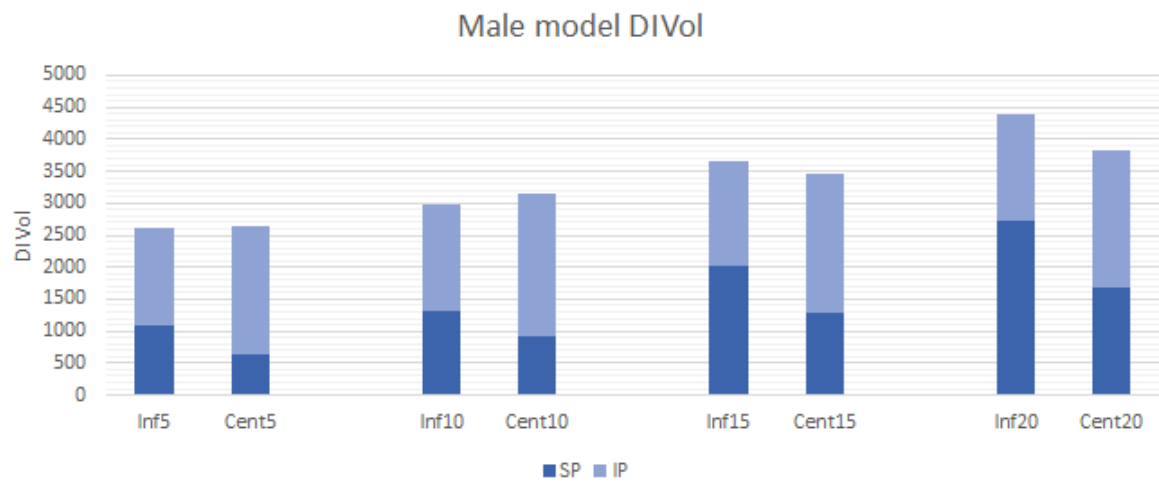
Figure 4.8: Damage distribution on the male bone models. From left to right, distances from the tip of the blade to the femoral head surface of 5, 10, 15 and 20 mm.

overload. The damage distribution follows the same pattern, albeit with a higher incidence. DIVol-SP was 207.12 on the normal load case, and 4361.2 on the overload case. These values represent, respectively, 26.4% and 57.5% of the total DIVol of the models.

The lower line in Figure 4.10 presents the damage distribution for the Fcent20 model with the same loading conditions referred before. In this case, DIVol-SP was 1754.2 on the normal load case, and 9093.0 on the overload case.



(a)



(b)

Figure 4.9: DIVol for both the SP and IP of all geometries for the (a) female and (b) male models.

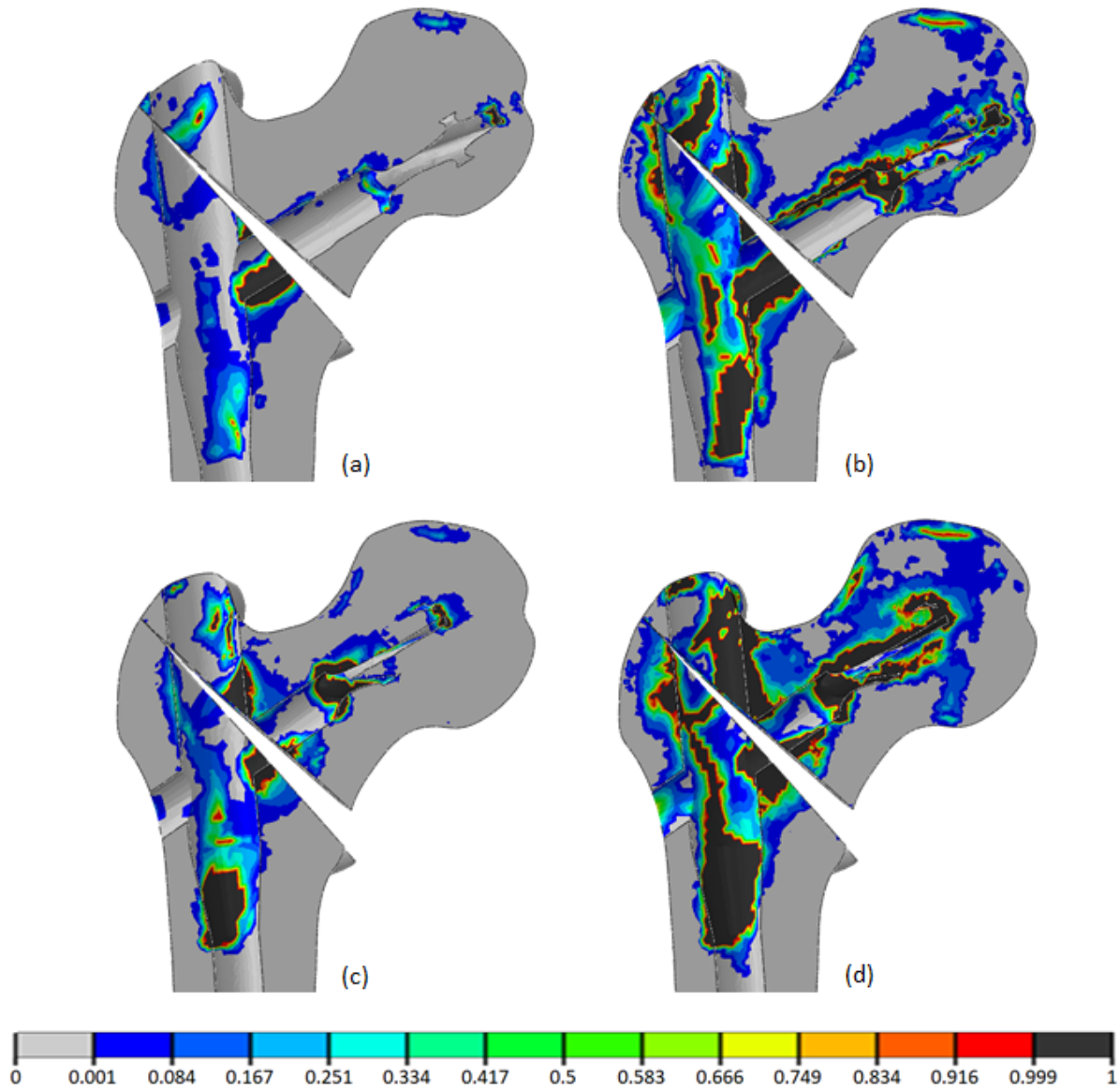


Figure 4.10: Comparison between the damage distribution on the Finf5 and Fcent20 model, using the normal loading scheme or a 100% overload. (a) Finf5 with normal loading; (b) Finf5 with a 100% overload; (c) Fcent20 with normal loading; (d) Fcent20 with a 100% overload

Chapter 5

Discussion

The objective of this work was to assess the risk of cut-out for several positions of the PFNA blade on the femoral head. To accomplish this, 3D finite element models were developed for both female and male bones, with an unstable 31-A2.2 fracture, and with the blade placed centrally in the anterior-posterior direction, as suggested in the literature. The position in the superior-inferior direction varied between a central and an inferior position, and the distance from the tip of the blade to the external surface of the femoral head, measured in straight line from the axis of the blade, was set at four discrete values between 5 and 20 mm. The model was coupled with a quasi-brittle damage model that evaluated and adapted the stiffness loss resulting from the yielding of the bone. Full loading was applied initially to the models in an iterative process until convergence of the damage distribution was reached.

Before evaluating the risk of cut-out of the models developed, and with the aim of gaining confidence on the damage model implemented, the results for the Finf5 geometry obtained for this work were compared to those obtained following the methodology by Vasconcelos [78] and Quental et al. [19]. Only the compressive damage regions were considered, for the sake of comparison, since these works only considered compressive yielded regions as damaged bone. The damage distribution was consistent with the regions with strain above the yield strain of these works, providing confidence in the damage model implementation. The residual differences on both distributions may be attributed to different yielding criteria used: while Vasconcelos and Quental et al. evaluated the minimum (compressive) principal strain, this work used an equivalent strain to take into consideration the total strain at each node; also, the yield strains considered were different.

In Figure 4.5, the evolution of the damage distribution in the bone with an increasing loading scheme is presented. It is possible to see that damage at the tip of the blade started from low loading values, together with some damage at the fracture region. This shows that these are the regions more prone to damage. As the loading increased, the damage propagated and its intensity increased, particularly at the tip of the blade, around the blade transition region and at the fracture region.

Although a central position in the anterior-posterior direction is consensually optimal for the positioning of the PFNA blade, no consensus exists yet on the best position in the superior-inferior direction. Arias-Blanco et al. [8], Hsueh et al. [11] and Konya and Verim [96] defended that the blade should be

placed centrally, while Lee et al. [15], Quental et al. [19] and Celik et al. [16] recommended an inferior position. From the results obtained for the female model, the inferior position was less prone to cut-out, since the DIVol-SP was lower than in the central positions for the same depth. For the male model, the central positions seemed safer than the inferior positions. This may be explained by differences in their density distribution. For the female model, the blade was always positioned in regions of low bone density, whereas for the male model, the central positioning of the blade placed it in a region of higher bone density than when placed inferiorly, as illustrated in Figure 5.1 for all models with a 5 mm distance from the tip of the blade to the femoral head surface. This may explain the higher safety in central positions suggested by the results for the male femur.

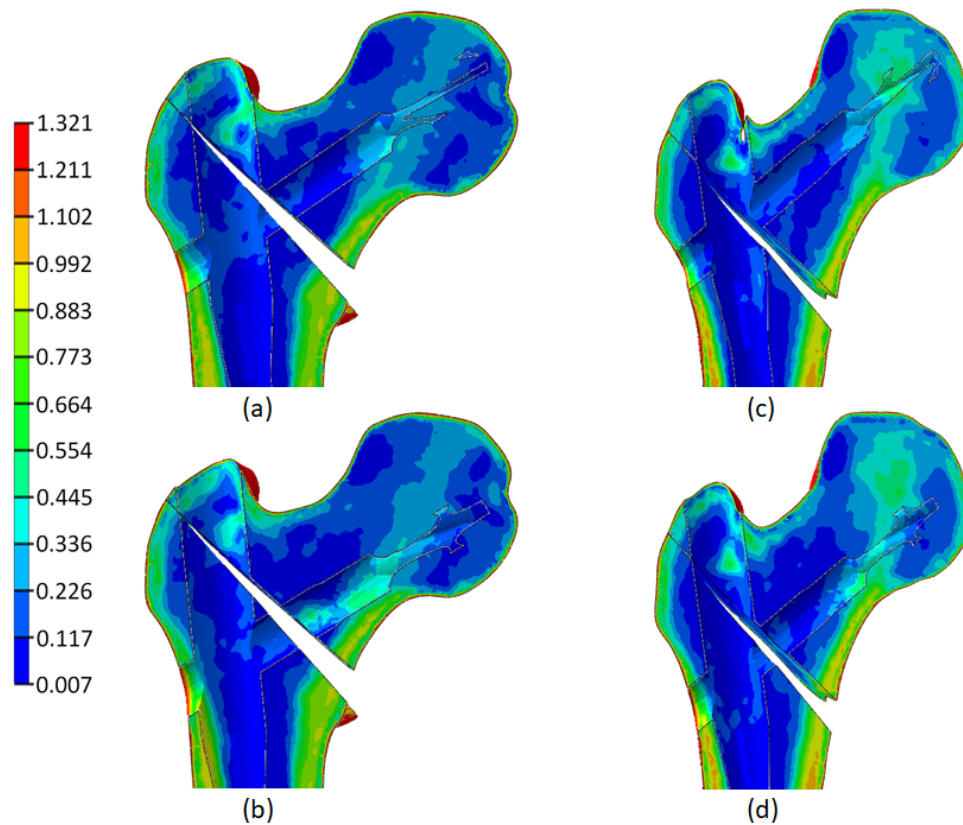


Figure 5.1: Bone density, in g cm^{-3} , for male and female, central and inferior models. (a) Fcent5; (b) Finf5; (c) Mcent5; (d) Minf5

The depth of placement of the blade was found to greatly influence the decrease of the risk of cut-out. For both male and female models, the higher the distance from the tip of the blade to the external surface of the femoral head (i.e., the less deep the placement), the higher the damage in the three main regions to be evaluated in the SP: at the tip of the blade; in the blade transition region; and in the fracture region. These are the same regions identified by Goffin et al. [18] and Quental et al. [19] as critical for the risk of cut-out. The visual inspection of damage distribution (cf. Figures 4.7 and 4.8) and the evolution of the DIVol-SP with the distance (cf. Figure 4.9) confirm the influence of the depth of the blade position on the risk of cut-out. This conclusion is verified for both central and inferior positions, partially contradicting the findings of Vasconcelos [78], who found no damage at the tip of the blade and around the blade

transition region for central geometries and argued that, for these geometries, no significant differences on the risk of cut-out were observed, suggesting that orthopaedic surgeons have a margin for error if the blade is inserted in this position. Based in the results obtained, the recommended depth of the blade is 5 mm. There are other effects that were not taken into consideration in this study, in particular medial perforations of the proximal femur [97]. Therefore, positioning the blade with a distance under 5 mm is not recommended, since this is the minimum suggested distance by the manufacturer [20].

Regarding the global blade positioning, while the results suggest inserting the blade as deep as possible, they are unable to identify which position is best along the superior-inferior direction. Nevertheless, from Figure 4.9, the difference of the risk of cut-out for different depths is higher than that for different superior-inferior positions. Also, using as example the female case results, a deep central position is less prone to cut-out than a less deep inferior position. These considerations suggest that the depth of the blade position is a more relevant indicator for the risk of cut-out than the blade position in the superior-inferior direction.

Unlike Quental et al. [19], the male models were found to present a higher risk of cut-out, having, for the same blade positions, higher DIVol than the female bones. Despite being discrepant, these results are supported by the literature, where there is generally no relationship reported between the patient's sex and the propensity to cut-out [98, 99].

The introduction of the damage model with stiffness reduction was responsible for an increase of the damaged area. All previous computational studies referred in Section 2.4.1 considered a single iteration simulation with full loading, making this the first work, to the author's knowledge, to apply an iterative damage model to investigate the risk of cut-out. This work is closer to the real case, since the yielding of bone takes effect in the stiffness reduction between iterations. Figure 4.6 shows that the damage increases along the iterations, even with the same load, because the stiffness is updated accordingly. The stiffness update forces the load to be redistributed, impacting damage and damage distribution in other undamaged bone regions. Another advantage of the damage model is that it allows handling nodes under tension and compression differently, and computing damage in both. Previous studies had only considered compressive damage for assessing the risk of cut-out [8, 15–19, 53, 78]. By also evaluating tensile damage, the damage model takes into account the fracture process, detecting microcracks due to high tensile strain [73, 76, 77].

The new fracture modelled in this work represents a poorer reduction of the fracture than those of Goffin et al. [18], Vasconcelos [78] and Quental et al. [19], introducing more instability in the system and a higher risk of cut-out [54]. This fracture geometry has not been mentioned previously in the literature, for what this work represents an advance in the studies of different trochanteric fractures.

The overload analyses, in Section 4.3.2, showed a significant increase in the risk of cut-out. DIVol-SP increased 21 times in the Finf5 case with a 100% load increment, and the percentage of DIVol-SP relative to the total DIVol went from 26.4% to 57.5%, more than duplicating – suggesting that, with excessive loading, the SP starts to gain more preponderance on the damage distribution over the IP. The overload analyses intended to evaluate incidents happening to the patients – while Heller et al. [32] loading conditions are a good approximation of the real forces exerted during gait under normal

conditions, incidents that are responsible for high impact (e.g. falls) may happen, leading to more severe loading in the proximal femur. Figure 4.10 presents damage above the entire length of the blade for the high load results, indicating the propensity of the femoral head to move down relatively to the screw, leading to a higher risk of the screw to cut-out of the superior region of the femoral head.

Despite its contributions, this work contains some limitations. Firstly, from a geometric point of view, only one female and one male femora were studied, with only one fracture geometry. Although the study would have benefited from having more femur models, the analysed femora fall within the typical geometries [19]. Nevertheless, different fracture geometries would have allowed to perceive the influence of this factor in the results. Regarding loading, only one loading case, representative of gait, was implemented in this work, limiting its applicability to everyday situations.

Regarding the implementation of the models, the damage model was only applied to the solid bone parts; nonetheless, since the shells are also bone tissues, the damage model could have been applied to these structures as well. Furthermore, other works implemented this damage model in Abaqus/Standard using a subroutine UMAT [73, 76, 77], while, in this work, the damage model was implemented using a MATLAB routine. Using UMAT allows for the damage model to be implemented directly in every increment of the Abaqus' Step, while the present approach computed damage only at the end of the step. With UMAT, the stiffness is updated several times in the same iteration, while, with the present implementation, the stiffness for a given iteration is constant [100]. Finally, the same works used an element deletion technique when critical damage was reached, allowing for the fracture to progress. In this work, the critical damaged nodes were maintained, with its Young's modulus only being reduced.

Chapter 6

Conclusions and future work

The goal of the present work was to assess the risk of cut-out for several positions of the PFNA blade on the femoral head. To accomplish that, 3D finite element models for both a female and a male femora with a PFNA implant were used. The position in the superior-inferior direction varied between a central and an inferior position, and the distance from the tip of the blade to the external surface of the femoral head varied between 5 and 20 mm. The model was coupled with a quasi-brittle damage model that evaluated and adapted the stiffness loss resulting from the yielding of the bone. Full loading was applied from beginning in an iterative process until convergence of the damage distribution was reached.

Overall, the depth of placement of the blade in the medial-lateral direction and its superior-inferior position were shown to have great influence in the risk of cut-out, with the medial-lateral position being the most relevant predictor. The best position to place the blade was found to be in the inferior (for the female bone) or central (for the male bone) regions, at a 5 mm distance from the femoral head surface. Bone critical damage was found to be predominant at the tip of the blade, around the blade's transition region and at the fracture region. Finally, the influence of higher loads than usual was found to represent a greater risk of cut-out.

To the author's knowledge, this is the first study to apply a damage model to a bone-implant system of a hip fracture, leading bone stiffness to be constantly adapting according to the damage distribution, and allowing the identification of the most critical areas on the bone. Nonetheless, some work remains to be done.

A larger number of femora should be considered in future studies. This would allow to investigate the reason behind the contradictory results for the two femora considered regarding the superior-inferior position. Also, different fracture geometries should be studied, to evaluate its influence in the recommended blade position and the risk of cut-out. Different loading cases should also be analysed (e.g. stair climbing), in order to have a broader knowledge on the risk of cut-out for everyday situations. Finally, concerning the implementation of the damage model, a kill-element technique should be implemented, in order to allow microcracks to progress.

References

- [1] M. N. Sarvi. Hip fracture: Anatomy, causes, and consequences. *IntechOpen*, November 2018. doi: 10.5772/intechopen.75946.
- [2] T. P. van Staa, E. M. Dennison, H. G. Leufkens, and C. Cooper. Epidemiology of fractures in England and Wales. *Bone*, 29(6):517–522, December 2001. doi: 10.1016/s8756-3282(01)00614-7.
- [3] S. Amin, S. J. Achenbach, E. J. Atkinson, S. Khosla, and L. J. Melton. Trends in fracture incidence: A population-based study over 20 years. *Journal of Bone and Mineral Research*, 29(3):581–589, March 2014. doi: 10.1002/jbmr.2072.
- [4] E. K. Osnes, C. M. Lofthus, H. E. Meyer, J. A. Falch, L. Nordsletten, I. Cappelen, and I. S. Kristiansen. Consequences of hip fracture on activities of daily life and residential needs. *Osteoporosis International*, 15(7):567–574, July 2004. doi: 10.1007/s00198-003-1583-0.
- [5] P. Kannus, J. Parkkari, H. Sievänen, A. Heinonen, I. Vuori, and M. Järvinen. Epidemiology of hip fractures. *Bone*, 81(1 Suppl):57S–63S, January 1996. doi: 10.1016/8756-3282(95)00381-9.
- [6] P. Carpintero, J. R. Caeiro, R. Carpintero, A. Morales, S. Silva, and M. Mesa. Complications of hip fractures: a review. *World Journal of Orthopedics*, 5(4):402–411, September 2014. doi: 10.5312/wjo.v5.i4.402.
- [7] S. Eberle, C. Gerber, G. von Oldenburg, F. Högel, and P. Augat. A biomechanical evaluation of orthopaedic implants for hip fractures by finite element analysis and in-vitro tests. *Proceedings of the Institution of Mechanical Engineers, Part H*, 224(10):1141–1152, October 2010. doi: 10.1243/09544119JEIM799.
- [8] A. Arias-Blanco, M. Marco, E. Giner, M. H. Miguélez, J. R. Caeiro-Rey, and R. Larraínzar-Garijo. The cut-out phenomenon in intertrochanteric femur fracture: analysis using a finite element model. *Revista de Osteoporosis y Metabolismo Mineral*, 13(1):21–31, 2021. doi: 10.4321/S1889-836X2021000100005.
- [9] A. J. Bojan, C. Beimel, G. Taglang, D. Collin, C. Ekholm, and A. Jönsson. Critical factors in cut-out complication after gamma nail treatment of proximal femoral fractures. *BMC Musculoskeletal Disorders*, 14(1), January 2013. doi: 10.1186/1471-2474-14-1.

- [10] H. Andruszkow, M. Frink, C. Frömke, A. Matityahu, C. Zeckey, P. Mommsen, S. Suntardjo, C. Krettek, and F. Hildebrand. Tip apex distance, hip screw placement, and neck shaft angle as potential risk factors for cut-out failure of hip screws after surgical treatment of intertrochanteric fractures. *International Orthopaedics*, 36(11):2347–2354, November 2012. doi: 10.1007/s00264-012-1636-0.
- [11] K.-K. Hsueh, C.-K. Fang, C.-M. Chen, Y.-P. Su, H.-F. Wu, and F.-Y. Chiu. Risk factors in cutout of sliding hip screw in intertrochanteric fractures: an evaluation of 937 patients. *International Orthopaedics*, 34:1273–1276, September 2010. doi: 10.1007/s00264-009-0866-2.
- [12] T. Fujii, S. Nakayama, M. Hara, W. Koizumi, T. Itabashi, and M. Saito. Tip-apex distance is most important of six predictors of screw cutout after internal fixation of intertrochanteric fractures in women. *JB & JS Open Access*, 2(4), December 2017. doi: 10.2106/JBJS.OA.16.00022.
- [13] R. Valentini, M. Martino, G. Piovan, G. D. Fabrizio, and G. Fancellu. Proximal cut-out in pertrochanteric femoral fracture. *Acta Biomedica*, 85(2):144–151, August 2014.
- [14] M. Büyükkuscu, S. Basilgan, A. Misir, A. Polar, and H. Basar. Factors associated with the development of screw cut-out after the fixation of intertrochanteric femoral fractures with a proximal femoral nail. *Journal of Health Sciences and Medicine*, 4(2):170–175, March 2021. doi: 10.32322/jhsm.860548.
- [15] P.-Y. Lee, K.-J. Lin, H.-W. Wei, J.-J. Hu, W.-C. Chen, C.-L. Tsai, and K.-P. Lin. Biomechanical effect of different femoral neck blade position on the fixation of intertrochanteric fracture: a finite element analysis. *Biomedical Engineering*, 61(3), September 2015. doi: 10.1515/bmt-2015-0091.
- [16] T. Celik, I. Mutlu, A. Ozkan, and Y. Kisioglu. Comparison of the lag screw placements for the treatment of stable and unstable intertrochanteric femoral fractures regarding trabecular bone failure. *Journal of Medical Engineering*, 2016, November 2016. doi: 10.1155/2016/5470798.
- [17] C. Liang, R. Peng, N. Jiang, G. Xie, L. Wang, and B. Yu. Intertrochanteric fracture: Association between the coronal position of the lag screw and stress distribution. *Asian Journal of Surgery*, 41(3):241–249, May 2018. doi: 10.1016/j.asjsur.2017.02.003.
- [18] J. M. Goffin, P. Pankaj, and A. H. Simpson. The importance of lag screw position for the stabilization of trochanteric fractures with a sliding hip screw: A subject-specific finite element study. *Journal of Orthopaedic Research*, 31(4):596–600, October 2012. doi: 10.1002/jor.22266.
- [19] C. Quental, S. Vasconcelos, J. Folgado, and F. Guerra Pinto. Influence of the PFNA screw position on the risk of cut-out in an unstable intertrochanteric fracture: a computational analysis. *Medical Engineering and Physics*, 97:70–76, October 2021. doi: 10.1016/j.medengphy.2021.10.001.
- [20] PFNA. *With Augmentation Option - Surgical Technique Guide*. DePuy Synthes Trauma, 2020. Available from: <https://ifu.depuysynthes.com/>.

- [21] M. R. Baumgaertner, S. L. Curtin, D. M. Lindskog, and J. M. Keggi. The value of the tip-apex distance in predicting failure of fixation of peritrochanteric fractures of the hip. *The Journal of Bone and Joint Surgery. American volume*, 77(7):1058–1064, July 1995. doi: 10.2106/00004623-199507000-00012.
- [22] R. L. Drake, A. W. Vogl, and A. W. M. Mitchell. *Gray's Anatomy for Students*. Elsevier, 4th edition, 2020.
- [23] S. J. Hall. *Basic Biomechanics*. McGraw-Hill, 6th edition, 2012.
- [24] Human anatomy planes. Internet, April 2019. Available from: <https://www.anatomynote.com/human-anatomy/gross-view-of-human-body/human-anatomy-planes/> [Cited October 19, 2021].
- [25] O. Jones. The hip joint. Internet, January 2019. Available from: <https://teachmeanatomy.info/lower-limb/joints/hip-joint/> [Cited October 13, 2021].
- [26] A. J. Sophia Fox, A. Bedi, and S. A. Rodeo. The basic science of articular cartilage: Structure, composition and function. *Sports Health*, 1(6):461–468, November 2009. doi: 10.1177/1941738109350438.
- [27] C. Battista. Hip anatomy. Internet, June 2021. Available from: <https://www.orthobullets.com/recon/12769/hip-anatomy> [Cited October 13, 2021].
- [28] M. Doblaré, J. M. García, and M. J. Gómez. Modelling bone tissue fracture and healing: a review. *Engineering Fracture Mechanics*, 71(13-14):1809–1840, September 2004. doi: 10.1016/j.engfracmech.2003.08.003.
- [29] D. H. Pahr and A. G. Reisinger. A review on recent advances in the constitutive modeling of bone tissue. *Current Osteoporosis Reports*, 18:696–704, October 2020. doi: 10.1007/s11914-020-00631-1.
- [30] N. M. B. K. Willems, G. E. J. Langenbach, V. Everts, and A. Zentner. The microstructural and biomechanical development of the condylar bone: A review. *The European Journal of Orthodontics*, 36(4):479–485, December 2013. doi: 10.1093/ejo/cjt093.
- [31] A. L. Ransom, M. A. Sinkler, and S. V. Nallamotheu. Anatomy, bony pelvis and lower limb, femoral muscles. StatPearls [Internet]. Treasure Island (FL): StatPearls Publishing, October 2021. Available from: <https://www.ncbi.nlm.nih.gov/books/NBK500008/> [Cited October 13, 2021].
- [32] M. O. Heller, G. Bergmann, J. P. Kassi, L. Claes, N. P. Haas, and G. N. Duda. Determination of muscle loading at the hip joint for use in pre-clinical testing. *Journal of Biomechanics*, 38(5): 1155–1163, May 2005. doi: 10.1016/j.jbiomech.2004.05.022.
- [33] M. Schuenke, E. Schulte, and U. Schumacher. *General Anatomy and Musculoskeletal System (THIEME Atlas of Anatomy)*. Thieme, 3rd edition, May 2020.

- [34] R. Mittal and S. Banerjee. Proximal femoral fractures: Principles of management and review of literature. *Journal of Clinical Orthopaedics and Trauma*, 3(1):15–23, June 2012. doi: 10.1016/j.jcot.2012.04.001.
- [35] T. Chesser, G. Chauhan, and M. Kelly. Management of hip fractures in the elderly. *Surgery*, 34(9):440–443, September 2016. doi: 10.1016/j.mpsur.2016.06.002.
- [36] Hip fractures. Internet, September 2021. Available from: https://www.amboss.com/us/knowledge/Hip_fractures/ [Cited October 14, 2021].
- [37] S. E. Sheehan, J. Y. Shyu, M. J. Weaver, A. D. Sodickson, and B. Khurana. Proximal femoral fractures: What the orthopedic surgeon wants to know. *RadioGraphics*, 35(5):1563–1584, July 2015. doi: 10.1148/rg.2015140301.
- [38] P. R. B. de Toledo Lourenço and R. E. S. Pires. Subtrochanteric fractures of the femur: update. *Revista Brasileira de Ortopedia*, 51(3):246–253, March 2016. doi: 10.1016/j.rboe.2016.03.001.
- [39] M. Butler, M. Forte, R. L. Kane, S. Joglekar, S. J. Duval, M. Swiontkowski, and T. Wilt. Treatment of common hip fractures. *Evidence Report/ Technology Assessment*, 184:1–85, August 2009.
- [40] H. B. Boyd and L. L. Griffin. Classification and treatment of trochanteric fractures. *Archives of Surgery*, 58(6):853–866, June 1949. doi: 10.1001/archsurg.1949.01240030864012.
- [41] M. Mokawem, P. Bobak, and J. Aderinto. The management of pertrochanteric fractures of the hip. *Orthopaedics and Trauma*, 26(2):112–123, April 2012. doi: <https://doi.org/10.1016/j.mporth.2012.04.001>.
- [42] M. E. Müller, S. Nazarian, P. Koch, and J. Schatzker. *The Comprehensive Classification of Fractures of Long Bones*. Springer-Verlag, 1990. doi: 10.1007/978-3-642-61261-9.
- [43] E. M. Evans. The treatment of trochanteric fractures of the femur. *The Journal of Bone and Joint Surgery - British volume*, 31B(2):190–203, May 1949.
- [44] J. S. Jensen and M. Michaelsen. Trochanteric femoral fractures treated with mclaughlin osteosynthesis. *Acta Orthopaedica Scandinavica*, 46(5):795–803, November 1975. doi: 10.3109/17453677508989266.
- [45] P. Adam. Treatment of recent trochanteric fracture in adults. *Orthopaedics & Traumatology: Surgery & Research*, 100(1 Suppl):S75–S83, February 2014. doi: 10.1016/j.otsr.2013.11.007.
- [46] A. Norrish. Proximal femoral fractures: Per- and intertrochanteric hip fractures. Handout. Published by AO Trauma.
- [47] A. L. Utrilla, J. S. Reig, F. M. Muñoz, and C. B. Tufanisco. Trochanteric gamma nail and compression hip screw for trochanteric fractures: a randomized, prospective, comparative study in 210 elderly patients with a new design of the gamma nail. *Journal of Orthopaedic Trauma*, 19(4): 229–233, April 2005. doi: 10.1097/01.bot.0000151819.95075.ad.

- [48] *DHS/DCS Dynamic Hip and Condylar Screw System. Designed to provide stable internal fixation. Technique Guide.* DePuy Synthes Trauma. Available from: <https://ifu.depuysynthes.com/>.
- [49] W. Yu, X. Zhang, X. Zhu, Z. Yu, Y. Xu, G. Zha, J. Hu, J. Yi, and Y. Liu. Proximal femoral nails anti-rotation versus dynamic hip screws for treatment of stable intertrochanteric femur fractures: an outcome analyses with a minimum 4 years of follow-up. *BMC Musculoskeletal Disorders*, 17 (222), May 2016. doi: 10.1186/s12891-016-1079-7.
- [50] L. Shen, Y. Zhang, Y. Shen, and Z. Cui. Antirotation proximal femoral nail versus dynamic hip screw for intertrochanteric fractures: A meta-analysis of randomized controlled studies. *Orthopaedics & Traumatology: Surgery & Research*, 99(4):377–383, June 2013. doi: 10.1016/j.otsr.2012.12.019.
- [51] J. Zou, Y. Xu, and H. Yang. A comparison of proximal femoral nail antirotation and dynamic hip screw devices in trochanteric fractures. *The Journal of International Medical Research*, 37(4): 1057–1064, July 2009. doi: 10.1177/147323000903700410.
- [52] S. A. Abdalbary. Partial weight bearing in hip fracture rehabilitation. *Future Science OA*, 4(1), January 2018. doi: 10.4155/fsoa-2017-0068.
- [53] J. M. Goffin, P. Pankaj, and A. H. Simpson. A computational study on the effect of fracture intrusion distance in three- and four-part trochanteric fractures treated with Gamma Nail and Sliding Hip Screw. *Journal of Orthopaedic Research*, 32(1), January 2014. doi: 10.1002/jor.22469.
- [54] F. Guerra Pinto, P. Dantas, R. Moreira, R. Mamede, and L. Branco Amaral. Complications relating to accuracy of reduction of intertrochanteric fractures treated with a compressive hip screw. *Hip International*, 20(2):221–228, April 2010. doi: 10.1177/112070001002000213.
- [55] A. C. Unger, E. Wilde, B. Kienast, C. Jürgens, and A. P. Schulz. Treatment of trochanteric fractures with the Gamma3 Nail - methodology and early results of a prospective consecutive monitored clinical case series. *The Open Orthopaedics Journal*, 8:466–473, December 2014. doi: 10.2174/1874325001408010466.
- [56] S. Papasimos, C. M. Koutsojannis, A. Panagopoulos, P. Megas, and E. Lambiris. A randomised comparison of AMBI, TGN and PFN for treatment of unstable trochanteric fractures. *Archives of Orthopaedic and Trauma Surgery*, 125(7):462–8, September 2005. doi: 10.1007/s00402-005-0021-5.
- [57] C. O'Donnell. Cut-out lag screw, neck of femur fracture gamma nail. Case study, Internet. Available from: <https://radiopaedia.org/cases/41480> [Cited October 19, 2021].
- [58] G. Caruso, M. Bonomo, G. Valpiani, G. Salvatori, A. Gildone, V. Lorusso, and L. Masari. A six-year retrospective analysis of cut-out risk predictors in cephalomedullary nailing for peritrochanteric fractures: Can the tip-apex distance (TAD) still be considered the best parameter? *Bone & Joint Research*, 6(8):481–488, August 2017. doi: 10.1302/2046-3758.68.BJR-2016-0299.R1.

- [59] A. Turgut, Önder Kalenderer, L. Karapinar, M. Kumbaraci, H. A. Akkan, and H. Ağuş. Which factor is most important for occurrence of cutout complications in patients treated with proximal femoral nail antirotation? retrospective analysis of 298 patients. *Archives of Orthopaedic and Trauma Surgery*, 136(5):623–630, May 2016. doi: 10.1007/s00402-016-2410-3.
- [60] P. Kane, B. Vopat, W. Heard, N. Thakur, D. Paller, S. Koruprolu, and C. Born. Is tip apex distance as important as we think? a biomechanical study examining optimal lag screw placement. *Clinical Orthopaedics and Related Research*, 472(8):2492–2498, August 2014. doi: 10.1007/s11999-014-3594-x.
- [61] P. R. T. Zuzyk, R. Zdero, S. Shah, M. Olsen, J. P. Waddell, and E. H. Schemitsch. Femoral head lag screw position for cephalomedullary nails: a biomechanical analysis. *Journal of Orthopaedic Trauma*, 26(7):414–421, July 2012. doi: 10.1097/BOT.0b013e318229acca.
- [62] P. Helwig, G. Faust, U. Hindenlang, A. Hirschmüller, L. Konstantinidis, C. Bahrs, N. Südkamp, and R. Schneider. Finite element analysis of four different implants inserted in different positions to stabilize an idealized trochanteric femoral fracture. *Injury*, 40(3):288–295, March 2009. doi: 10.1016/j.injury.2008.08.016.
- [63] X. Huang, B. Yu, Y. Gu, and Z. Li. Biomechanical comparison of dynamic hip screw and gamma nail for the treatment of unstable trochanteric fractures: A finite element study. *International Journal of Clinical and Experimental Medicine*, 10(5):7867–7874, May 2017.
- [64] G.-X. Yuan, Y.-H. Shen, B. Chen, and W.-B. Zhang. Biomechanical comparison of internal fixations in osteoporotic intertrochanteric fracture. a finite element analysis. *Saudi Medical Journal*, 33(7):732–739, July 2012.
- [65] J. Lemaitre. *A Course on Damage Mechanics*. Springer-Verlag Berlin Heidelberg, 2nd edition, 1996. doi: 10.1007/978-3-642-18255-6.
- [66] J.-L. Chaboche. Continuous damage mechanics — a tool to describe phenomena before crack initiation. *Nuclear Engineering and Design*, 64(2):233–247, April 1981. doi: 10.1016/0029-5493(81)90007-8.
- [67] D. Dapaah, R. Badaoui, A. Bahmani, J. Montesano, and T. Willett. Modelling the micro-damage process zone during cortical bone fracture. *Engineering Fracture Mechanics*, 224, February 2020. doi: 10.1016/j.engfracmech.2019.106811.
- [68] D. Garcia, P. K. Zysset, M. Charlebois, and A. Curnier. A 1d elastic plastic damage constitutive law for bone tissue. *Archive of Applied Mechanics*, 80(5):543–555, May 2010. doi: 10.1007/s00419-009-0382-2.
- [69] P. K. Zysset and U. Wolfram. A rate-independent continuum model for bone tissue with interaction of compressive and tensile micro-damage. *Journal of the Mechanical Behavior of Biomedical Materials*, 74:448–462, October 2017. doi: 10.1016/j.jmbbm.2017.07.008.

- [70] J. J. Schwiedrzik and P. K. Zysset. An anisotropic elastic-viscoplastic damage model for bone tissue. *Biomechanics and Modeling in Mechanobiology*, 12(2):201–213, April 2013. doi: 10.1007/s10237-012-0392-9.
- [71] I. T. Haider, J. Goldak, and H. Frei. Femoral fracture load and fracture pattern is accurately predicted using a gradient-enhanced quasi-brittle finite element model. *Medical Engineering & Physics*, 55:1–8, May 2018. doi: 10.1016/j.medengphy.2018.02.008.
- [72] T. P. Ng, S. S. R. Koloor, J. R. P. Sjuansjah, and M. R. A. Kadir. Assessment of compressive failure process of cortical bone materials using damage-based model. *Journal of the Mechanical Behavior of Biomedical Materials*, 66:1–11, February 2017. doi: 10.1016/j.jmbbm.2016.10.014.
- [73] R. Hambli, A. Bettamer, and S. Allaoui. Finite element prediction of proximal femur fracture pattern based on orthotropic behaviour law coupled to quasi-brittle damage. *Medical Engineering & Physics*, 34(2):202–210, March 2012. doi: 10.1016/j.medengphy.2011.07.011.
- [74] C. Qu, S.-W. Yu, X.-Q. Feng, and Z.-X. Hao. Damage model of bone under mechanical and electromagnetic loadings. *Computational Materials Science*, 57:89–93, May 2012. doi: 10.1016/j.commatsci.2011.06.037.
- [75] M. Ovesy, B. Voumard, and P. K. Zysset. A nonlinear homogenized finite element analysis of the primary stability of the bone–implant interface. *Biomechanics and Modeling in Mechanobiology*, 17:1471–1480, June 2018. doi: 10.1007/s10237-018-1038-3.
- [76] R. Hambli. A quasi-brittle continuum damage finite element model of the human proximal femur based on element deletion. *Medical & Biological Engineering & Computing*, 51(1-2):219–231, November 2013. doi: 10.1007/s11517-012-0986-5.
- [77] R. Hambli and S. Allaoui. A robust 3D finite element simulation of human proximal femur progressive fracture under stance load with experimental validation. *Annals of Biomedical Engineering*, 41(12):2515–2527, July 2013. doi: 10.1007/s10439-013-0864-9.
- [78] S. Vasconcelos. Influence of the femoral head screw position on the risk of cut out in trochanteric fractures: a computational analysis. Master’s thesis, Instituto Superior Técnico, September 2020.
- [79] T. L. Arthur Moore and L. J. Gibson. Microdamage accumulation in bovine trabecular bone in uniaxial compression. *Journal of Biomechanical Engineering*, 124(1):63–71, February 2002. doi: 10.1115/1.1428745.
- [80] G. P. Parsamian. *Damage mechanics of human cortical bone*. PhD thesis, West Virginia University, 2001.
- [81] S. Nagaraja, T. L. Couse, and R. E. Guldberg. Trabecular bone microdamage and microstructural stresses under uniaxial compression. *Journal of Biomechanics*, 38(4):707–716, April 2005. doi: 10.1016/j.jbiomech.2004.05.013.

- [82] U. Wolfram, H.-J. Wilke, and P. K. Zysset. Damage accumulation in vertebral trabecular bone depends on loading mode and direction. *Journal of Biomechanics*, 44(6):1164–1169, April 2011. doi: 10.1016/j.jbiomech.2011.01.018.
- [83] H. H. Bayraktar, E. F. Morgan, G. L. Niebur, G. E. Morris, E. K. Wong, and T. M. Keaveny. Comparison of the elastic and yield properties of human femoral trabecular and cortical bone tissue. *Journal of Biomechanics*, 37(1):27–35, January 2004. doi: 10.1016/S0021-9290(03)00257-4.
- [84] D. van Embden, M. S. Gaston, L. A. Bailey, and A. H. R. W. Simpson. Trochanteric femoral fracture classification: Relevance of the fracture line angle, a radiological study. *International Journal of Orthopaedics*, 2(2):250–255, April 2015. doi: 10.6051/j.issn.2311-5106.2015.02.55.
- [85] N. K. Knowles, J. M. Reeves, and L. M. Ferreira. Quantitative computed tomography (QCT) derived bone mineral density (BMD) in finite element studies: a review of the literature. *Journal of Experimental Orthopaedics*, 3(36), December 2016. doi: 10.1186/s40634-016-0072-2.
- [86] B. L. Riggs, J. Melton III, R. A. Robb, J. J. Camp, E. J. Atkinson, J. M. Peterson, P. A. Rouleau, C. H. McCollough, M. L. Bouxsein, and S. Khosla. Population-based study of age and sex differences in bone volumetric density, size, geometry, and structure at different skeletal sites. *Journal of Bone and Mineral Research*, 19(12):1945–1954, December 2004. doi: 10.1359/jbmr.040916.
- [87] J. Tohka. Partial volume effect modeling for segmentation and tissue classification of brain magnetic resonance images: A review. *World Journal of Radiology*, 6(11):855–864, November 2014. doi: 10.4329/wjr.v6.i11.855.
- [88] A. D. A. Souza, J. K. Udupa, and P. K. Saha. Volume rendering in the presence of partial volume effects. *Medical Imaging*, May 2002. doi: 10.1117/12.466974.
- [89] C. Quental, J. Folgado, M. Comenda, J. Monteiro, and M. Sarmiento. Primary stability analysis of stemless shoulder implants. *Medical Engineering & Physics*, 81:22–29, July 2020. doi: 10.1016/j.medengphy.2020.04.009.
- [90] S. Gupta, F. C. T. van der Helm, and F. van Keulen. The possibilities of uncemented glenoid component—a finite element study. *Clinical Biomechanics*, 19(3):292–302, March 2004. doi: 10.1016/j.clinbiomech.2003.12.002.
- [91] E. Schileo, F. Taddei, A. Malandrino, L. Cristofolini, and M. Viceconti. Subject-specific finite element models can accurately predict strain levels in long bones. *Journal of Biomechanics*, 40(13): 2982–2989, April 2007. doi: 10.1016/j.jbiomech.2007.02.010.
- [92] E. F. Morgan, H. H. Bayraktar, and T. M. Keaveny. Trabecular bone modulus–density relationships depend on anatomic site. *Journal of Biomechanics*, 36:897–904, July 2003. doi: 10.1016/S0021-9290(03)00071-X.
- [93] S. Sowmianarayanan, A. Chandrasekaran, and R. Krishna Kumar. Finite element analysis of a subtrochanteric fractured femur with dynamic hip screw, dynamic condylar screw, and proximal

- femur nail implants – a comparative study. *Proceedings of the Institution of Mechanical Engineers, Part H*, 222(1):117–127, February 2008. doi: 10.1243/09544119JEIM156.
- [94] G. Bergmann, F. Graichen, and A. Rohlmann. Hip joint loading during walking and running, measured in two patients. *Journal of Biomechanics*, 26(8):969–990, August 1993. doi: 10.1016/0021-9290(93)90058-m.
- [95] *Abaqus Analysis User's Manual*. Dassault Systèmes.
- [96] M. N. Konya and O. Verim. Numerical optimization of the position in femoral head of proximal locking screws of Proximal Femoral Nail system; biomechanical study. *Balkan Medical Journal*, 34(5):425–431, September 2017. 10.4274/balkanmedj.2016.0732.
- [97] M. Nayak, R. Yadav, V. Ganesh, and V. Digge. An unusual case of femoral head perforation following fixation with proximal femoral nail antirotation (PFNA-II) for an unstable intertrochanteric fracture: Case report and literature review. *Trauma Case Reports*, 20, February 2019. doi: 10.1016/j.tcr.2019.100178.
- [98] L. Murena, A. Moretti, F. Meo, E. Saggioro, G. Barbati, C. Ratti, and G. Canton. Predictors of cut-out after cephalomedullary nail fixation of pertrochanteric fractures: a retrospective study of 813 patients. *Archives of Orthopaedic and Trauma Surgery*, 138(3):351–359, March 2018. doi: 10.1007/s00402-017-2863-z.
- [99] K. De Bruijn, D. den Hartog, W. Tuinebreijer, and G. Roukema. Reliability of predictors for screw cutout in intertrochanteric hip fractures. *The Journal of Bone and Joint Surgery. American volume*, 94(14):1266–1272, July 2012. doi: 10.2106/JBJS.K.00357.
- [100] P. Bandeira. A continuum-damage model for advanced composites. Master's thesis, Faculty of Engineering of the University of Porto, August 2005.

Appendix A

Minimum stiffness sensitivity analysis

A sensitivity analysis for Young's modulus value assigned to the lowest value of density in the bone is shown in figure A.1. For doing so, the Finf5 model simulation was performed using a minimum stiffness for bone of 0.01 MPa, and a different simulation for the same model was performed with a minimum stiffness of 0.1 MPa. Both simulations were performed using the Convergence Analysis strategy for loading, and converged after 7 iterations to a tolerance of 5% in relative deviation of DIVol. The DIVol of the bone after each iteration was compared for both models, as shown in Figure A.1. The relative deviation of the simulation with higher minimum stiffness relatively to the other one is also presented in the figure.

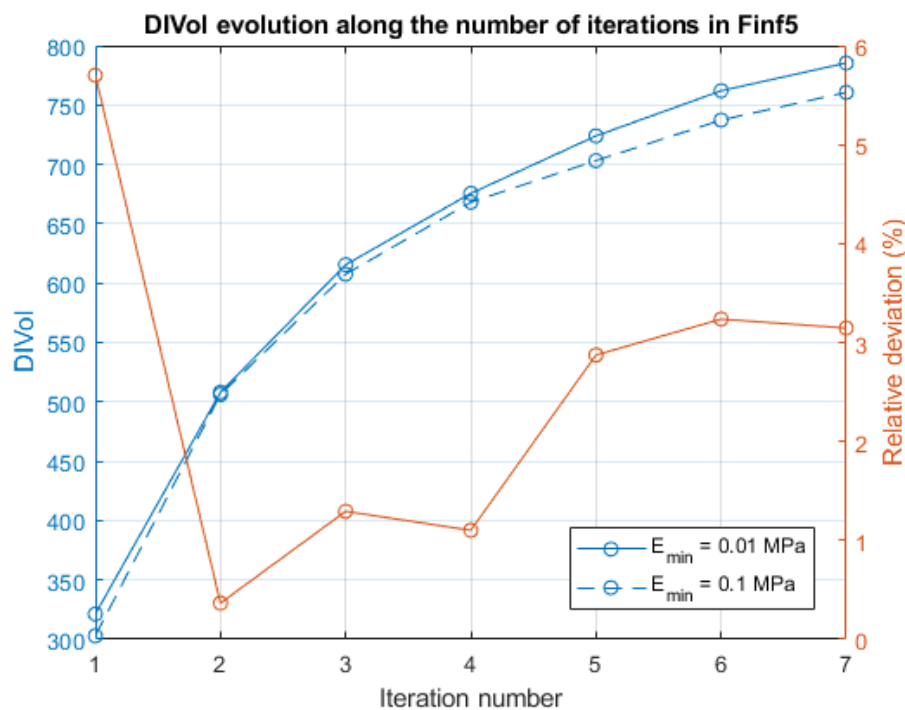


Figure A.1: Minimum stiffness sensitivity analysis.

The relative deviation between both results starts at 5.7%, decreasing afterwards to smaller values, with a relative maximum in 3.2%. Therefore, and because the relative deviation does not exceed the 5%

defined as DIVol deviation tolerance for convergence, it is concluded that the increase of the minimum stiffness after convergence issues is possible without compromising the results.